DISSERTATION

ELECTRICAL IMPEDANCE TOMOGRAPHY WITH CALDERÓN'S METHOD IN TWO AND THREE DIMENSIONS

Submitted by

Kwancheol Shin

Department of Mathematics

In partial fulfillment of the requirements

For the Degree of Doctor of Philosophy

Colorado State University

Fort Collins, Colorado

Summer 2020

Doctoral Committee:

Advisor: Jennifer L. Mueller

Margaret Cheney
Olivier Pinaud
Mahmoud Hussam

ABSTRACT

ELECTRICAL IMPEDANCE TOMOGRAPHY WITH CALDERÓN'S METHOD IN TWO AND THREE DIMENSIONS

Electrical impedance tomography (EIT) is a non-invasive imaging technique in which electrical measurements on the electrodes attached to the boundary of a subject are used to reconstruct the electrical properties of the subject. That is, voltage data arising from currents applied on the boundary are used to reconstruct the conductivity distribution in the interior.

Calderón's method is a direct linearized reconstruction method for the inverse conductivity problem with the attributes that it can provide absolute images with no need for forward modeling, reconstructions can be computed in real-time, and both conductivity and permittivity can be reconstructed.

In this three-paper dissertation, first, an explicit relationship between Calderón's method and the D-bar method is provided, facilitating a “higher-order" Calderón's method in which a correction term is included, derived from the relationship to the D-bar method. Furthermore, a method of including a spatial prior is provided. These advances are demonstrated on tank data collected with the ACE1 EIT system.

On the other hand, it has been demonstrated that various EIT reconstruction algorithms are very sensitive to the measurement and incorrect modeling of the boundary shape. Calderón's method has been implemented with correct boundary shape, but the exact location of the electrodes are disregarded as they are assumed to be spaced uniformly in angle. In the second body of work, Calderón's method is implemented with a new expansion technique which enables the use of the correct location of the electrodes as well as the shape of the boundary resulting in improved absolute images. We test our new algorithm with experimental data collected with the ACE1 EIT system.

Finally, the first implementation of Calderón's method on a 3-D cylindrical domain with data collected on a portion of the boundary is provided. The effectiveness of the method to localize inhomogeneities in the plane of the electrodes and in the z-direction is demonstrated on simulated and experimental data.

ACKNOWLEDGEMENTS

I would like to thank my advisor, Jennifer Mueller. Thank you for supporting me and teaching me the real world of mathematics. Thank you for engaging deeply with my work by answering all the questions I had very promptly, at any time, through tons of email exchanges and in-person meetings. Thank you for allowing me and supporting me to take part in many international conferences from where I could be motivated and learned a lot. Thank professor Joo-Han Yoon for encouraging me to study abroad and helping me all the time. Thank you to my committee, Margaret Cheney, Olivier Pinaud and Mahmoud Hussam for teaching me, for all questions and suggestions, and for encouraging me to continue to work. Thank you to my roommate James for taking care of me for five years, helping me to get adjusted and encouraging me to work. Thank Tom and Vickie for helping me all the time and spending time with me with a lot of outdoor activities.

Thank dad, mom, brothers and sister for everything.

TABLE OF CONTENTS

LIST OF FIGURES

Chapter 1

Introduction

1.1 What is EIT?

Electrical Impedance Tomography (EIT) is an imaging modality that aims to recover the impedance of a body by making use of electrical measurements on the surface of the body. Electrodes are placed on the surface of the body and low-frequency currents are applied on the electrodes. The currents then induce voltage distributions on the electrodes which are measured. These current-voltage distributions on the surface of the body are the data for the recovery of the impedance.

The mathematical equation that governs the EIT problem can be obtained from Maxwell's equation [55]. The equation is often called the conductivity equation which is in the form of the generalized Laplace equation:

$$\nabla \cdot [(\sigma(x) + i\omega\epsilon(x))\nabla u(x)] = 0, \tag{1.1}$$

where x is the spatial variable, i is $\sqrt{-1}$, ω is the angular frequency of the alternating current, σ is the conductivity, ϵ is the electric permittivity and u is the electric potential. The forward problem is to determine $u(x)$ when $\sigma,\ \epsilon$, and either the current or voltage distribution on the boundary of the body is given. The inverse problem is then to determine σ and ϵ when the current to voltage data on the boundary is given.

1.2 Applications

EIT has several advantages over other imaging modalities. It is cost-effective, portable, non-ionizing, and the fast electronics enable the monitoring of a time-varying object. EIT has many applications in different environments. It is used to construct tomographic images of the flow of a

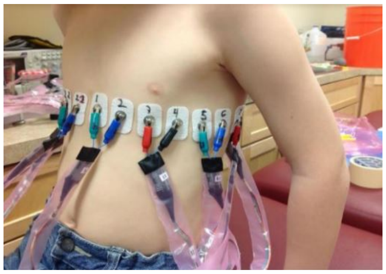

(A)

(B)

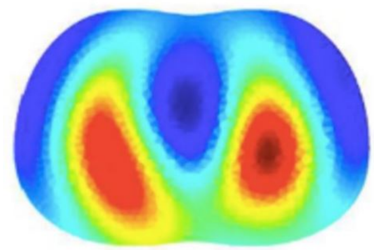

(C)

Figure 1.1: (A): EIT data collection from the subject. (B): The EIT system in CSU. (C): The reconstructed image showing the heart and two lungs.

fluid in the pipeline, concrete structures, and detection of leaks from buried pipes [42]. EIT is also used for geophysical prospection.

EIT is also applicable for medical imaging since human organs and tissues have very different electrical properties [44]. Compared to the CT-scan, EIT is free of radiation, low cost, and portable. The application to the early detection of breast cancer can be found in [19,38,45,50,67,72,83]. In mammography, there are a lot of false positives due to the microcalcifications: 80% of biopsies turn out to be benign. On the other hand, cancerous breast tissue is two to four times more conductive than the healthy breast tissue, [43,44,69,73]. It is shown in [66] that the combination of EIT with X-ray tomography enhances the sensitivity and specificity of the detection of breast cancer.

One of the most promising medical applications of EIT is pulmonary imaging. The conductivity of lung tissue with air in it is about 0.4 mS/cm. It is considerably less conductive than other tissue such as the heart(2.3-6.3 mS/cm), spine(0.05 mS/cm), and blood(6.07 mS/cm). See [32,55]. The existence of tumors or fluid in the lung changes the conductivity in that region considerably. This enables EIT to be used for imaging pulmonary ventilation [29–31, 40, 81], perfusion [11,53,70,77] and cardiac imaging [63,64].

Figure 1.1 shows how the EIT systems produdes a thoracic image. The images are taken at the EIT laboratory in CSU. (A) is the picture of data collection from a subject. (B) is the ACE1 EIT system in CSU. (C) is the reconstructed image showing the heart (blue region in the middle) and two lungs (red region on both sides).

1.3 Modeling of EIT

1.3.1 The Dirichlet-to-Neumann map

With equation (1.1), we consider two boundary conditions on the boundary $\partial\Omega$ of the body Ω in $\mathbb{R}^2$ or $\mathbb{R}^3$. The application of a voltage distribution f on the boundary corresponds to

$$u(x) = f(x), \quad x \in \partial\Omega. \tag{1.2}$$

This is called the Dirichlet condition and equations (1.1) and (1.2) constitute a Dirichlet problem in the case when the impedance $\gamma(x) = \sigma(x) + i\epsilon(x)$ is known. We measure the induced current density distribution j on the boundary and this corresponds to

$$j(x) = \gamma(x)\frac{\partial u}{\partial \nu}(x), \quad x \in \partial\Omega, \tag{1.3}$$

where ν denotes the unit outer normal to $\partial\Omega$. This is called the Neumann boundary condition, and equations (1.1) and (1.3) constitute the Neumann problem in the case when $\gamma(x)$ is known. In the absence of current sources or sinks in the body, by the conservation of charge, the current density is conserved over the boundary:

$$\int_{\partial\Omega} \gamma \frac{\partial u}{\partial \nu} \mathrm{d}s = 0,$$

where $\mathrm{d}s$ denotes surface measure. The *Dirichlet-to-Neumann (DN)* map takes the Dirichlet condition to the Neumann condition. Because of the practical implication of the data, this mapping is also called the voltage-to-current density map and is denoted by Λ_γ,

$$\Lambda_\gamma : u|_{\partial\Omega} \longrightarrow \gamma \frac{\partial u}{\partial \nu}\bigg|_{\partial\Omega}.$$

If $\gamma \in L^\infty(\Omega)$ is strictly positive almost everywhere in Ω, it is shown in [41] that there is a constant C that depends only on $\partial\Omega$ and γ such that, for all $f \in H^{\frac{1}{2}}(\partial\Omega)$,

$$\| \Lambda_\gamma(f) \|_{H^{-\frac{1}{2}}(\partial\Omega)} = \inf_{\| g \|_{H^{\frac{1}{2}}(\partial\Omega)} = 1} \left| \int_{\partial\Omega} \gamma \frac{\partial u}{\partial \nu} g \mathrm{d}s \right| \leq C \| f \|_{H^{\frac{1}{2}}(\partial\Omega)},$$

which means that the linear operator Λ_γ is bounded between the following Sobolev spaces:

$$\Lambda_\gamma : H^{\frac{1}{2}}(\partial\Omega) \longrightarrow H^{-\frac{1}{2}}(\partial\Omega).$$

Knowing Λ_γ is equivalent to knowing the current density on the boundary arising from any given voltage distribution on the boundary.

1.3.2 The Neumann-to-Dirichlet map

Let $u \in H^1(\Omega)$ be the unique solution of (1.1) with the application of the current density j on the boundary

$$\gamma \frac{\partial u}{\partial \nu} = j \text{ on } \partial\Omega, \tag{1.4}$$

satisfying the choice of ground condition $\int_{\partial\Omega} u \mathrm{d}s = 0$. The *Neumann-to-Dirichlet (ND) map* takes the given current-density distribution to the voltage distribution. This mapping is also called the current-density-to-voltage map and is denoted by $\mathcal{R}_\gamma$,

$$\mathcal{R}_\gamma : \gamma \frac{\partial u}{\partial \nu}\bigg|_{\partial\Omega} \longrightarrow u|_{\partial\Omega}.$$

$\mathcal{R}_\gamma : \tilde{H}^{-\frac{1}{2}}(\partial\Omega) \rightarrow \tilde{H}^{\frac{1}{2}}(\partial\Omega)$ is bounded where $\tilde{H}^s$ is the space of H^s functions with mean value zero. The ND map $\mathcal{R}_\gamma$ is self-adjoint, smoothing, and compact.

1.3.3 Nonlinearity of EIT

For practical applications, EIT is a difficult problem mainly because it is ill-posed [1] and nonlinear. While the DN map is a linear operator because the governing conductivity equation is linear, the forward map $\gamma \mapsto \Lambda_\gamma$ is nonlinear. To show this, we consider the weak form of the DN map as follows. Let $u_{\gamma,f}$ denote the weak solution in $H^1(\partial\Omega)$ of the differential equation $\nabla \cdot (\gamma \nabla u_{\gamma,f}) = 0$ with $u_{\gamma,f}|_{\partial\Omega} = f$. We define a linear functional $\Lambda_\gamma f$ defined on $g \in H^{\frac{1}{2}}(\partial\Omega)$ by an inner product on $\partial\Omega$ as

$$\langle \Lambda_\gamma f, g \rangle = \int_\Omega \gamma \nabla u_{\gamma,f} \cdot \nabla v dx, \tag{1.5}$$

where $v \in H^1(\Omega)$ is any function such that $v|_{\partial\Omega} = g$ in the trace sense. This gives a weak definition of the map Λ_γ on functions $f \in H^{\frac{1}{2}}(\partial\Omega)$ and it is well defined since if we let $v', v \in H^1(\Omega)$ be two functions such that $v'|_{\partial\Omega} = v|_{\partial\Omega} = g$, then $v' = v + \phi$ for $\phi \in H_0^1(\partial\Omega)$, and therefore $\int_\Omega \gamma \nabla u_{\gamma,f} \cdot \nabla v' dx = \int_\Omega \gamma \nabla u_{\gamma,f} \cdot \nabla v dx + \int_\Omega \gamma \nabla u_{\gamma,f} \cdot \nabla \phi dx = \int_\Omega \gamma \nabla u_{\gamma,f} \cdot \nabla v dx$ by the definition of the weak solution. If Ω has C^∞ boundary and $\gamma \in C^\infty(\overline{\Omega})$, then the map Λ_γ restricts to a linear map from $C^\infty(\partial\Omega)$ to $C^\infty(\partial\Omega)$ which satisfies for $f \in C^\infty(\partial\Omega)$, $\Lambda_\gamma f = \gamma \partial_\nu u_{\gamma,f}|_{\partial\Omega}$. To this end, let f be a function in $C^\infty(\partial\Omega)$. Then by the regularity theorem for the elliptic differential operator, $u_{\gamma,f}$ is now a $C^\infty(\Omega)$ function so that we can think of $\gamma \frac{\partial u_{\gamma,f}}{\partial \nu}$ in $\partial\Omega$ in the strong sense. Let g be any function in $H_0^1(\Omega)$. By integration by part,

$$\langle \Lambda_\gamma f, g \rangle = \int_\Omega \gamma \nabla u_{\gamma,f} \cdot \nabla v \mathrm{d}x = \int_{\partial\Omega} \gamma \frac{\partial u_{\gamma,f}}{\partial \nu} g \mathrm{d}s.$$

Since g is arbitrary in $C^\infty(\partial\Omega)$, this shows that $\Lambda_\gamma f = \gamma \partial_\nu u_{\gamma,f}|_{\partial\Omega}$ for $f \in C^\infty(\partial\Omega)$. From the definition of the DN map Λ_γ in (1.5), we consider the quadratic form Q_γ for the DN map Λ_γ as a linear functional on $f \in H^{\frac{1}{2}}(\partial\Omega)$,

$$Q_\gamma(f) = \langle \Lambda_\gamma f, f \rangle = \int_\Omega \gamma |\nabla u_{\gamma,f}|^2 \mathrm{d}x. \tag{1.6}$$

$Q_\gamma(f)$ represents the power necessary to maintain an electrical potential f on $\partial\Omega$ and knowing Q_γ is equal to knowing Λ_γ. Since for fixed f, $u_{\gamma,f}$ depends on γ,

$$\begin{aligned} Q_{\gamma_1+\gamma_2}(f) = \langle \Lambda_{\gamma_1+\gamma_2} f, f\rangle &= \int_\Omega (\gamma_1+\gamma_2)|\nabla u_{\gamma_1+\gamma_2,f}|^2 \mathrm{d}x \\ &= \int_\Omega \gamma_1 |\nabla u_{\gamma_1+\gamma_2,f}|^2 dx + \int_\Omega \gamma_2 |\nabla u_{\gamma_1+\gamma_2,f}|^2 \mathrm{d}x \end{aligned}$$

is not equal to

$$\begin{aligned} (Q_{\gamma_1}+Q_{\gamma_2})(f) &= Q_{\gamma_1}(f) + Q_{\gamma_2}(f) \\ &= \langle \Lambda_{\gamma_1} f, f\rangle + \langle \Lambda_{\gamma_2} f, f\rangle \\ &= \int_\Omega \gamma_1 |\nabla u_{\gamma_1,f}|^2 \mathrm{d}x + \int_\Omega \gamma_2 |\nabla u_{\gamma_2,f}|^2 \mathrm{d}x. \end{aligned}$$

Therefore the forward map $\gamma \mapsto \Lambda_\gamma$, or equivalently $\gamma \mapsto Q_\gamma$ is not linear. This means that for a fixed applied voltage distribution, the measured current density is a nonlinear function of the conductivity distribution in Ω. This is in contrast to the X-ray tomography and makes EIT difficult.

1.4 Theory of Calderón's method

In [12], Calderón posed EIT problem for the first time and proved the solvability of the linearized problem by making use of certain complex exponential harmonic functions which are now known as *Complex Geometrical Optics (CGO) solutions*. This motivated the construction of CGO solutions [74, 75], and their usage. A review of CGO solutions can be found in [76]. The D-bar method of which the name comes from the use of the $\overline{\partial}$ operator also uses CGO solutions. The comprehensive details of the theory and numerical implementations of this method can be found in [55]. While Calderón's method is a linearized method, the D-bar method solves the full nonlinear inverse problem directly. It was shown in [46] that Calderón's method is a linearization of the D-bar method.

Calderón considered the following problem. Let Ω be a bounded domain in $\mathbb{R}^n,\ n \geq 2$, with Lipschitz boundary $\partial\Omega$, and γ be a real bounded measurable function in Ω with a positive lower bound. Let the differential operator L_γ be

$$L_\gamma(\omega) = \nabla \cdot (\gamma \nabla w),$$

acting on functions of $H^1(\Omega)$, and the quadratic form $Q_\gamma(\phi)$ be

$$Q_\gamma(\phi) = \int_\Omega \gamma |\nabla \omega|^2 \mathrm{d}x,$$

where ϕ is the trace on $\partial\Omega$ of a function $\omega \in H^1(\mathbb{R}^n)$ with $L_\gamma(\omega) = 0$ in Ω. Then, as explained in (1.6), knowing the quadratic form Q_γ is equivalent to knowing the DN map.

The forward problem is then to solve the differential equation $L_\gamma(\omega) = 0$ with the coefficient function γ and either the Dirichlet or Neumann boundary condition is given. The associated inverse problem is to find γ when Q_γ is given. More specifically, Calderón considered two problems: Is γ uniquely determined by Q_γ? If that is the case, can γ be expressed by Q_γ?

To formulate this problem mathematically, he introduced the following norms in the space of functions ϕ on $\partial\Omega$ and in the space of quadratic forms Q_γ,

$$\begin{aligned} \| \phi \|^2 &= \int_\Omega |\nabla u|^2 \mathrm{d}x \quad ;\ u|_{\partial\Omega} = \phi, \quad \triangle u = 0 \quad \text{in} \quad \Omega \\ \| Q_\gamma \| &= \sup_{\| \phi \| \leq 1} |Q_\gamma(\phi)|. \end{aligned}$$

Consider the map

$$\Phi : \gamma \to Q_\gamma.$$

This forward map is bounded and analytic on the subset of $L^\infty(\Omega)$ consisting of functions that are real and have a positive lower bound.

The uniqueness question is equivalent to whether the map Φ is injective or not. Instead of proving the injectivity of Φ, he proved that the *Fréchet* derivative $d\Phi|_{\gamma=const.}$ is indeed injective, that is, if $\gamma(x) = \gamma_0 + \delta(x)$ where $\| \delta(x)\|_{L^\infty}$ is sufficiently small and γ_0 is a constant, then γ can be nearly determined by Q_γ.

Let us sketch the proof of the injectivity of $d\Phi|_{\gamma=const.}$. We assume $\gamma_0 = 1$ for simplicity of the proof. Express the solution of the equation

$$L_\gamma(\omega) = \nabla \cdot (\gamma \nabla \omega) = 0, \quad \omega|_{\partial\Omega} = \phi, \quad \gamma = 1 + \delta$$

as $\omega = u + v$, where $\triangle u = L_1 u = 0$, $u|_{\partial\Omega} = \phi$. Then

$$L_\gamma(\omega) = L_{1+\delta}(u + v) = L_1(v) + L_\delta(v) + L_\delta(u) = 0.$$

Let G be a bounded inverse of $L_1 : H^1(\Omega) \to H^{-1}(\Omega)$. Then from the above equation,

$$v + GL_\delta v = -GL_\delta u.$$

Consider L_1 and L_δ as linear map from $H^1(\Omega)$ to $H^{-1}(\Omega)$ such that for $u \in H^1(\Omega)$,

$$< L_\delta u, v >= \int_\Omega \delta \nabla u \cdot \nabla v \mathrm{d}x,$$

for any $v \in H_0^1(\Omega)$. Here, $< \cdot, \cdot >$ represents the pairing between $H^{-1}(\Omega)$ and $H_0^1(\Omega)$. Then by the Cauchy-Schwartz inequality,

$$\left| \int_\Omega \delta \nabla u \cdot \nabla v dx \right| \le \| \delta \|_{L^\infty(\Omega)} \| u \|_{H^1(\Omega)} \| v \|_{H^1(\Omega)},$$

and this implies that $\| L_\delta u \|_{H^{-1}(\Omega)} \le \| \delta \|_{L^\infty(\Omega)} \| u \|_{H^1(\Omega)}$, and therefore $\| L_\delta \|_{L(H^1(\Omega), H^{-1}(\Omega))} \le \| \delta \|_{L^\infty(\Omega)}$. Let $\| G\|_{L(H^{-1}(\Omega), H_0^1(\Omega))} = A$. Then $\| GL_\delta \| \le A \| \delta \|_{L^\infty}$. We also note that since u satisfies $L_1 u = 0$ in Ω and $u|_{\partial\Omega} = \phi$ on $\partial\Omega$, by the theory of elliptic differential equations, $\| u \|_{H^1(\Omega)} \le C \| \phi \|_{H^{1/2}(\Omega)}$ for some constant C that depends only on Ω. Therefore, if $A \| \delta \|_{L^\infty} \le$

1, the Neumann series

$$v=-\left[\sum_{0}^{\infty}(-1)^j(GL_\delta)^j\right](GL_\delta u)$$

converges and

$$\| v\|_{H^1(\Omega)}\le\frac{A\|\delta\|_{L^\infty}\|\phi\|_{H^{1/2}(\partial\Omega)}}{1-A\|\delta\|_{L^\infty(\Omega)}}. \tag{1.7}$$

Expand the map Φ near 1 by using the *Fréchet* derivative of Φ at $\gamma=1$ in the direction δ so that

$$\Phi(\gamma)=\Phi(1)+d\Phi|_{\gamma=1}(\delta(x))+o(\|\delta\|_{L^\infty}).$$

Let the map $D: L^\infty(\Omega)\to H^{-\frac{1}{2}}(\partial\Omega)$ be a linear map such that for $\delta\in L^\infty(\Omega)$ and $\phi\in H^{\frac{1}{2}}(\partial\Omega)$,

$$[D(\delta)](\phi)=\int_D\delta|\nabla u|^2dx,\ \text{ where } u|_{\partial\Omega}=\phi,\quad \triangle u=0,\ u\in H^1(\Omega).$$

Then $D(\delta)$ is a bounded map and

$$\begin{aligned}
&\|Q_{1+\delta}-Q_1-D(\delta)\|_{H^{-\frac{1}{2}}(\partial\Omega)}\\
&=\sup_{\|\phi\|_{H^{\frac{1}{2}}(\partial\Omega)}=1}|[Q_{1+\delta}-Q_1-D(\delta)](\phi)|\\
&=\sup_{\|\phi\|_{H^{\frac{1}{2}}(\partial\Omega)}=1}\left|\int_\Omega\gamma|\nabla w|^2-|\nabla u|^2-\delta|\nabla u|^2\mathrm{d}x\right|\\
&=\sup_{\|\phi\|_{H^{\frac{1}{2}}(\partial\Omega)}=1}\left|\int_\Omega(1+\delta)|\nabla w|^2-|\nabla u|^2-\delta|\nabla u|^2\mathrm{d}x\right|\\
&=\sup_{\|\phi\|_{H^{\frac{1}{2}}(\partial\Omega)}=1}\int_\Omega(1+\delta)(2\nabla u\cdot\nabla v+|\nabla v|^2)\mathrm{d}x\\
&=\sup_{\|\phi\|_{H^{\frac{1}{2}}(\partial\Omega)}=1}\int_\Omega(2\delta\nabla u\cdot\nabla v+\gamma|\nabla v|^2)\mathrm{d}x\\
&=\sup_{\|\phi\|_{H^{\frac{1}{2}}(\partial\Omega)}=1}2\|\delta\|_{L^\infty}\|\nabla u\|_{L^2(\Omega)}\|v\|_{H^1(\Omega)}+\|\gamma\|_{L^\infty(\Omega)}\|v\|^2_{H^1(\Omega)}
\end{aligned}$$

$$
\leq \sup_{\|\phi\|_{H^{\frac{1}{2}}(\partial\Omega)}=1} \left\{ 2C\|\delta\|_{L^\infty(\Omega)}\|\phi\|_{H^{\frac{1}{2}}(\Omega)} \frac{A\|\delta\|_{L^\infty}\|\phi\|_{H^{\frac{1}{2}}(\Omega)}}{1 - A\|\delta\|_{L^\infty(\Omega)}} \right.
$$

$$
\left. + \|\gamma\|_{L^\infty(\Omega)} \left(\frac{A\|\delta\|_{L^\infty(\Omega)}\|\phi\|_{H^{\frac{1}{2}}(\Omega)}}{1 - A\|\delta\|_{L^\infty(\Omega)}} \right)^2 \right\}
$$

$$
= 2C\|\delta\|_{L^\infty} \frac{A\|\delta\|_{L^\infty(\Omega)}}{1 - A\|\delta\|_{L^\infty(\Omega)}} + \|\gamma\|_{L^\infty(\Omega)} \left\{ \frac{A\|\delta\|_{L^\infty(\Omega)}}{1 - A\|\delta\|_{L^\infty(\Omega)}} \right\}^2 = o(\|\delta\|_{L^\infty(\Omega)}).
$$

Therefore, D is the desired *Fréchet* derivative

$$
d\Phi|_{\gamma=1} \colon \delta \to d\Phi|_{\gamma=1}(\delta).
$$

To show that $d\Phi|_{\gamma=1}$ is injective, it is enough to show that $\delta = 0$ if $\int_D \delta|\nabla u|^2 \mathrm{d}x = 0$ for all u with $\triangle u = 0$. To this end, assume $\int_D \delta|\nabla u|^2 \mathrm{d}x = 0$ for all harmonic function u. Note for the two harmonic functions

$$
u_1 = e^{\pi i k\cdot x + \pi a\cdot x} \quad \text{and} \quad u_2 = e^{\pi i k\cdot x - \pi a\cdot x}, \tag{1.8}
$$

where $a, k \in \mathbb{R}^n$ with $k \cdot a = 0$ and $|k| = |a|$, that

$$
\nabla u_1 \cdot \nabla u_2 = (i\pi k + \pi a)u_1 \cdot (i\pi k - \pi a)u_2 = -2\pi^2|k|^2 e^{2\pi i k\cdot x}.
$$

Since $u_1 + u_2$ is also harmonic,

$$
\begin{aligned}
0 &= \int_\Omega \delta|\nabla(u_1 + u_2)|^2 \mathrm{d}x \\
&= \int_\Omega \delta(|\nabla u_1|^2 + 2\nabla u_1 \cdot \nabla u_2 + |\nabla u_1|^2)\mathrm{d}x \\
&= 2\int_\Omega \delta(\nabla u_1 \cdot \nabla u_2)\mathrm{d}x \\
&= -4\pi^2|k|^2 \int_\Omega \delta(x) e^{2\pi i k\cdot x}\mathrm{d}x.
\end{aligned}
$$

Since k is arbitrary, this implies $\delta(x) = 0$.

Now, to express γ in terms of Q_γ, we set again $\gamma = 1 + \delta$ and introduce the bilinear form

$$B(\phi_1, \phi_2) = \frac{1}{2}\left[Q_\gamma(\omega_1 + \omega_2) - Q_\gamma(\omega_1) - Q_\gamma(\omega_2)\right] \tag{1.9}$$

and setting $\omega_j = u_j + v_j$, $j = 1, 2$, $\triangle u_j = 0$, $u_j|_{\partial\Omega} = \phi_j$, we obtain

$$B(\phi_1, \phi_2) = \int_\Omega (1+\delta)(\nabla u_1 \cdot \nabla u_2) + \delta\left[(\nabla u_1 \cdot \nabla v_2) + (\nabla u_2 \cdot \nabla v_1)\right] + (1+\delta)(\nabla v_1 \cdot \nabla v_2)\mathrm{d}x. \tag{1.10}$$

As the notation already suggests, we use the special harmonic functions u_1 and u_2 in (1.8). Substituting u_1 and u_2 into equation (1.10), we get

$$\hat{\gamma}(k) = \hat{F}(k) + R(k)$$

where $\hat{\gamma}(k)$ is the Fourier transform of γ extended to be zero outside Ω, that is,

$$\hat{\gamma}(k) = \int_{\mathbb{R}^n} \gamma(x)\chi_\Omega(x) e^{2\pi i x\cdot k}\mathrm{d}x$$

and

$$\hat{F}(k) = -\frac{1}{2\pi^2|k|^2} B\left(e^{i\pi(k\cdot x)+\pi(a\cdot x)}, e^{i\pi(k\cdot x)-\pi(a\cdot x)}\right)$$

which is known in terms of Q_γ as in equation (1.9) or in terms of the DN map Λ_γ, because

$$\begin{aligned}
B(\phi_1, \phi_2) &= \frac{1}{2}\int_\Omega \gamma|\nabla(\omega_1 + \omega_2)|^2 - \gamma|\nabla\omega_1|^2 - \gamma|\nabla\omega_2|^2\mathrm{d}x \\
&= \frac{1}{2}\int_\Omega 2\gamma(\nabla\omega_1 \cdot \nabla\omega_2)\mathrm{d}x \\
&= \int_{\partial\Omega} \omega_1 \gamma \frac{\partial\omega_2}{\partial\nu}\mathrm{d}s = \int_{\partial\Omega} \phi_1 \Lambda_\gamma(\phi_2)\mathrm{d}s.
\end{aligned}$$

From the inequality (1.7), we can estimate

$$|R(k)| \leq C \| \delta \|_{L^\infty}^2 e^{2\pi r|k|},$$

provided that $A \| \delta \|_{L^\infty} \leq 1 - \epsilon$, where C depends only on Ω, ϵ and the radius r of the smallest sphere containing Ω. Notice that this bound for the remainder term $R(k)$ grows exponentially as $|k|$ gets large, so that taking the inverse Fourier transformation of $\hat{F}(k)$ with large $|k|$ values would not be a good approximation of $\gamma(x)$. That is, since large $|k|$ values correspond to the high-frequency nature of $\gamma(x)$, including values of $\hat{F}(k)$ for large $|k|$ would result in highly oscillatory reconstructions for γ. Therefore, we need to use only the values of $\hat{F}(k)$ within a certain bounded region. In order to obtain this threshold, pick α, such that $1 < \alpha < 2$, then for

$$|k| \leq \frac{2-\alpha}{\pi r} \log \frac{1}{\| \delta \|_{L^\infty}}, \tag{1.11}$$

the error term has a bound, as in [8],

$$\begin{aligned} |R(k)| &\leq C \| \delta \|_{L^\infty}^2 e^{2\pi r \frac{2-\alpha}{2\pi r} \log \frac{1}{\| \delta \|_\infty}} \\ &= C \| \delta \|_\infty^2 e^{\log \left(\frac{1}{\| \delta \|_\infty} \right)^{2-\alpha}} \\ &= C \| \delta \|_\infty^2 \| \delta \|_\infty^{\alpha-2} \\ &= C \| \delta \|_\infty^{\alpha}. \end{aligned}$$

This enables us to conclude that $\hat{F}(k)$ is a good approximation for $\hat{\gamma}(k)$ in the region (1.11) when $\| \delta \|_\infty$ is small.

As we assume that γ is only a measurable function with a positive lower bound and a small perturbation from a constant in the L^∞ norm sense, it does not necessarily have to be a smooth function. Therefore, in order to avoid the Gibbs phenomenon in the reconstruction, introduce a mollifier η such that $\hat{\eta} \in C^{\infty},\ supp(\hat{\eta}) \subset \{|k| \leq 1\}$, $\hat{\eta}(0) = 1$, and let $\eta_t(k) = t^n \eta(tk)$. Then

$$\hat{\gamma}(k)\hat{\eta}\left(\frac{k}{t}\right) = \hat{F}(k)\hat{\eta}\left(\frac{k}{t}\right) + R(k)\hat{\eta}\left(\frac{k}{t}\right), \tag{1.12}$$

and taking the inverse Fourier transform gives

$$(\gamma * \eta_t)(x) = (F * \eta_t)(x) + \rho(x), \tag{1.13}$$

where * denotes convolution, and a bound for ρ is

$$|\rho(k)| \leq C \| \delta \|_{L^\infty}^{\alpha} \left[\log \frac{1}{\| \delta \|_{L^\infty}}\right]^n,$$

which converges to zero as $\| \delta \|_{L^\infty}$ goes to zero. This bound implies that for small $\| \delta \|_{L^\infty}$, the inverse Fourier transform of $\hat{F}(k)\hat{\eta}(k/t)$ is a good approximation for $\gamma * \eta_t$. Also, if $\| \delta \|_{L^\infty}$ is small then t is large and η_t has a narrow and high peak at the origin so that $\gamma * \eta_t$ itself is a good approximation for γ.

The practical implementation of Calderón's method was first done in [8] with experimental data collected on a circular tank. The implementation of this method on elliptic domain was first done in [56]. The implementation of this method on subject-specific domains including experimental data collected on a chest shaped tank and human data was first done in [58]. In [14], electrical admittivities in 2-D circular domain was recovered with Calderón's method and two-terminal/electrode excitation strategies. Reconstruction of complex conductivity by Calderón's method on subject-specific domains can be found in [57].

1.5 Overview of Papers

This dissertation comes in the form of three papers. In the first paper, I developed and implemented a method to include *a priori* information about organ locations and conductivities in Calderón's method. I developed the second order Calderón's method based on a study of the connection between Calderón's method and the D-bar method. These methods are tested with experimental tank data. In the second paper, I developed a numerical technique for including the correct location of the electrodes in Calderón's method and tested this method on experimental tank data. In the third paper, I developed a three dimensional Calderón's method on the cylindrical geometry and tested the algorithm on both simulated and experimental tank data.

1.5.1 Paper 1: A second order Calderón's method with a correction term and a priori information

The goal of this paper is to develop an improved two dimensional Calderón's method with a second order correction term and *a prior* information. Also included is a technique for improving the absolute image. We first study the explicit relationship between Calderón's method and the D-bar method and explain how Calderón's method linearizes the D-bar method. From the relationship, we find one second order correction term to Calderón's method toward the D-bar method and suggest *the second order Calderón's method.* For the inclusion of prior information, we first assume that we know the approximate location of inclusions and approximated constant conductivity for each inclusion. By using that information, we construct a spatial prior. The technique basically consists of appending the Fourier transform of the spatial prior to $\hat{F}(k)$, and then taking the inverse Fourier transform of the appended $\hat{F}(k)$. In order to reduce the Gibbs phenomena in the absolute image, we suggest a technique of subtracting the Fourier transform of the background constant conductivity from $\hat{F}(k)$. We test our algorithms for many experimental tank data including complex valued admittivity targets and demonstrate that the algorithms improve the reconstruction.

1.5.2 Paper 2: Calderón's method with the correct electrode location for the absolute image

The goal of this paper is to implement the exact location of electrodes to Calderón's method. While Calderón's method has been implemented with experimental non-circular tank data [56–58], the exact location of electrodes was ignored by assuming that they are spaced uniformly in angle.

In this paper, we propose a new technique of computing $\hat{F}(k)$ by expanding the CGO solutions directly to the applied current and measured voltage data. With this new approach, we are able to make use of the exact location of electrodes to Calderón's method. We test our algorithm on a chest shaped tank data demonstrating that our algorithm improves the absolute image significantly.

1.5.3 Paper 3: Three dimensional Calderón's method for EIT on the cylindrical geometry

The goal of this paper is to develop the three dimensional Calderón's method on the cylindrical geometry. We make use of the same expansions of CGO solutions as the expansions in paper 2. The geometry of the body of the object is the cylinder having multiple layers of electrodes and the approach is fully three dimensional, not stacking two-dimensional reconstructed images together. We test our algorithm on various simulated data with or without noise having two or four layers of electrodes. This is the first direct 3D reconstruction algorithm to be implemented in the cylindrical geometry on experimental or simulated data. The only other direct 3D algorithm to have been implemented on experimental data is the implementation of Calderón's method for the mammography geometry [10]. With simulated data, we see that the algorithm is capable of locating the targets not only horizontally but also vertically. We also test our algorithm with the experimental cylinder tank data with two layers of electrodes. In this paper, the simulated data was provided by Sanwar Uddin Ahmad using his finite element code. The formulation and numerical solution of the inverse problem was developed and programmed by the author.

Chapter 2

Paper 1: A second order Calderón's method with a correction term and a priori information

Calderón's method is a direct linearized reconstruction method for the inverse conductivity problem with the attributes that it can provide absolute images with no need for forward modeling, reconstructions can be computed in real time, and both conductivity and permittivity can be reconstructed. In this work, an explicit relationship between Calderón's method and the D-bar method is provided, facilitating a "higher-order" Calderón's method in which a correction term is included, derived from the relationship to the D-bar method. Furthermore, a method of including a spatial prior is provided. These advances are demonstrated on tank data collected with the ACE1 EIT system.

Keywords: electrical impedance tomography, inverse problems, Calderón's method.

Submitted to: *Inverse Problems*

2.1 Introduction

Calderón's 1980 paper *On an inverse boundary value problem* [12] has inspired several decades of research on the inverse conductivity problem. In this work, he proved that the linearized problem has a unique solution and proposed a direct method of reconstruction. Electrical impedance tomography, or EIT, is the primary application of the inverse conductivity problem, with applications in medical imaging, geophysics, and nondestructive testing. Calderón's proof and reconstruction method utilized special harmonic functions, now known as *complex geometrical optics* (CGO) solutions that have been generalized in the D-bar family of direct reconstruction algorithms for EIT. Calderón's method has, however, been slow to find its way to practical implementation in EIT. The first numerical implementation for Calderón's method was in [8] for experimental EIT data collected on a saline-filled tank and on a healthy human subject reconstructed on a circular domain. This implementation was extended in [56] to account for non-circular but symmetric domains, demonstrating the effects primarily on elliptical domains and was implemented in real time in 2-D on subject-specific domains in [57, 58]. However, as is the case with most reconstruction algorithms in EIT, due to the severe ill-posedness of the inverse problem, the reconstructions are low resolution and sensitive to noise in the data. One approach to improve the low-resolution blurred images characteristic of EIT is to include prior information in the reconstruction algorithm. This has proved successful in iterative methods [6, 7, 21, 22, 24–26, 71, 78] and in the D-bar method [2–5]. In the D-bar method, an effective means of including *a priori* spatial information about the unknown conductivity is to append the scattering transform computed from the data with a scattering transform computed from the conductivity prior.

In this work, we derive an explicit connection between Calderón's method and the D-bar method, beyond what was shown in [46], motivating the addition of a weighted higher order term to Calderón's method, which is both easy to compute and improves the spatial resolution and accuracy of the reconstructed conductivity values. Although the second order term is derived from the 2D D-bar method based on [60], the terms in the second order method are well-defined for complex-valued conductivities, and so we include examples from simulated and experimental data with a permittivity component illustrating its effectiveness. D-bar methods for reconstructing a complex conductivity are based on 2×2 elliptic systems of first-order PDE's [27, 36, 37], and therefore the derivation would be quite different from the method presented here, which makes use of the already established connection between the real-valued D-bar method and Calderón's method [46]. We invite others to consider such an approach.

Also introduced here is a method for including *a priori* information in the reconstruction algorithm, inspired by the technique proposed in [4] for the D-bar method. This is the first time a prior has been included in Calderón's method, and we apply it to the second-order method for both real and complex-valued conductivities. A method of including *a priori* spatial information for complex-valued conductivities in the 2-D D-bar method based on [27, 36, 37] was introduced in [3].

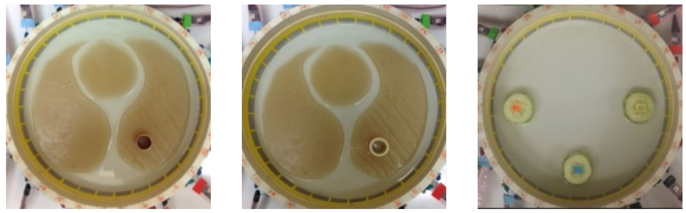

(A) Case (i) (B) Case (ii) (C) Case (iii)

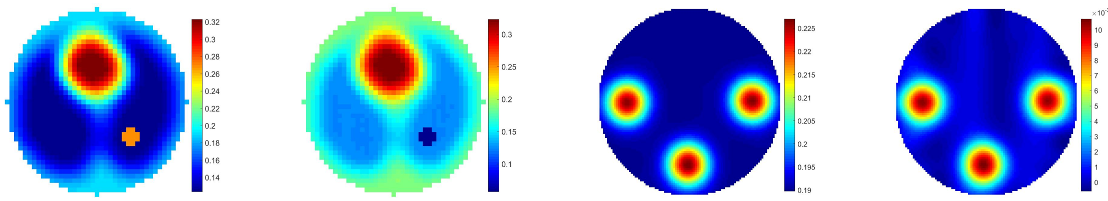

(D) Reference (i) (E) Reference (ii) (F) Reference (iii-R) (G) Reference (iii-I)

Figure 2.1: The three experimental data sets and reference images. Case (i): an agar heart and lungs in a saline bath with a copper pipe in one lung. Case (ii): an agar heart and lungs in a saline bath with a PVC pipe in one lung. Case (iii): three slices of cucumber in a saline bath. Figure (D) is a reference image for Case (i), Figure (E) is a reference image for Case (ii). Figure (F) and Figure (G) are the real part and the imaginary part reference images for Case (iii). Those reference images are used for the SSIM measures later.

Also included in this paper is a technique to minimize the effect of the Gibb's phenomena in the reconstruction of absolute images. The results of the higher order Calderón's method with a spatial prior are demonstrated on EIT data collected on a saline-filled tank with agar and cucumber targets as shown in Figure 2.1.

The paper is organized as follows. Section 2.2 includes the mathematical model for the inverse conductivity problem, the equations of Calderón's method, and the 2-D D-bar method for real-valued conductivities based on the constructive uniqueness proof in [60] that has been developed as a practical reconstruction algorithm (see [55,68] and references therein). The relationship between Calderón's method and the D-bar method and the derivation of the second order Calderón's method are found in Section 2.3. Calderón's method with a spatial prior is introduced in Section 2.4. Finally, the experimental results and discussion are found in Section 2.5.

2.2 Background

2.2.1 Governing equations

The inverse problem of electrical impedance tomography is modeled as follows. Let $\Omega \in \mathbb{R}^2$ be a bounded domain. The electrical potential $u(x)$ and electrical admittivity distribution $\gamma(x)$ defined on $\overline{\Omega}$ satisfy the generalized Laplace equation

$$\nabla \cdot (\gamma(x)\nabla u(x)) = 0, \quad x \in \Omega, \tag{2.1}$$

where $\gamma(x) = \sigma(x) + i\omega\epsilon(x)$, where σ is the conductivity, ω is the frequency of the applied alternating current, and ϵ is the permittivity of the medium. The application of a current density distribution j on the boundary corresponds to the Neumann boundary condition,

$$\gamma(x)\frac{\partial u}{\partial \nu}(x) = j(x), \quad x \in \partial\Omega,$$

where ν denotes the outward normal to $\partial\Omega$. The voltage f that arises on the boundary of Ω corresponds to the Dirichlet boundary condition,

$$u(x)|_{\partial\Omega} = f(x), \quad x \in \partial\Omega.$$

The current-density to voltage mapping is known as the Neumann-to-Dirichlet map. However, in the mathematical literature, it is typically the Dirichlet-to-Neumann, or voltage-to-current density map, that is used in proofs and algorithm development. Denoted by Λ_γ, it is given by

$$\Lambda_\gamma : u|_{\partial\Omega} \to \gamma\frac{\partial u}{\partial \nu}\bigg|_{\partial\Omega},$$

and the inverse problem is to find the unknown $\gamma(x)$ based on the knowledge of Λ_γ. Note that in practice, the boundary conditions in the model are usually replaced with conditions that take into account the discrete nature of the electrodes on the boundary and their interaction with the medium known as *contact impedance*. The reader is referred to [17, 18, 55] for the derivation, study, and implementation, respectively, of the Complete Electrode Model for EIT. Here, as in Calderón's method, we utilize Λ_γ as described above.

2.2.2 Calderón's method

Calderón assumes that the admittivity is of the form $\gamma(x) = 1 + \delta(x)$ where $\| \delta \|_{L^\infty(\Omega)}$ is small. The CGO solutions are given by $\phi_1(x; k, a) = \exp[\pi \mathrm{i}(x \cdot k) + \pi(a \cdot x)]$ and $\phi_2(x; k, a) = \exp[\pi \mathrm{i}(x \cdot k) - \pi(a \cdot x)]$, where k, $a \in \mathbb{R}^2$ are nonphysical frequency variables such that $|k| = |a|$ and $k \cdot a = 0$ that enable the two functions be harmonic, that is, $\triangle\phi_1 = \triangle\phi_2 = 0$. Calderón's idea is to use these two harmonic functions and the fact that when $\| \delta \|_{L^\infty(\Omega)}$ is small, the potentials arising from applied voltages $\phi_i (i = 1, 2)$ are small perturbations from ϕ_i in $H^1(\Omega)$. Calderón defines

$$\omega_i = u_i + v_i \text{ in } \Omega, \quad \omega_i|_{\partial\Omega} = \phi_i \text{ on } \partial\Omega, \;\; u_i \in H^1(\Omega), \;\; v_i \in H^1_0(\Omega)$$

for $i = 1, 2$, where $u_i = \phi_i$. By the definition of Λ_γ, integration by parts, and the conductivity equation,

$$\begin{aligned}
\int_{\partial\Omega} \phi_1 \Lambda_\gamma \phi_2 \mathrm{d}s(x) &= \int_{\partial\Omega} w_1 \gamma \frac{\partial \omega_2}{\partial \nu} \mathrm{d}s(x) \\
&= \int_\Omega \gamma \nabla\omega_1 \cdot \nabla\omega_2 \mathrm{d}x \\
&= \int_\Omega \gamma \nabla u_1 \cdot \nabla u_2 + \delta(\nabla u_1 \cdot \nabla v_2 + \nabla u_2 \cdot \nabla v_1) + \gamma \nabla v_1 \cdot \nabla v_2 \mathrm{d}x. \\
&= -2\pi^2 |k|^2 \int_\Omega \gamma(x) \exp[2\pi \mathrm{i} x \cdot k] \, \mathrm{d}x + \tilde{E}(k),
\end{aligned}$$

where $\tilde{E}(k)$ is the last three terms in the third line. By dividing by $-2\pi^2|k|^2$, we get

$$\int_\Omega \gamma(x) \exp[2\pi \mathrm{i} x \cdot k] \, \mathrm{d}x = -\frac{1}{2\pi^2|k|^2} \int_{\partial\Omega} \phi_1 \Lambda_\gamma \phi_2 \mathrm{d}s(x) + \frac{\tilde{E}(k)}{2\pi^2|k|^2}. \tag{2.2}$$

Thus, neglecting the remainder term $E(k) = \frac{\tilde{E}(k)}{2\pi^2|k|}$, we get

$$\hat{\gamma}(k) \approx -\frac{1}{2\pi^2|k|^2}\int_{\partial\Omega}\phi_1\Lambda_\gamma\phi_2 \mathrm{d}s(x) \equiv \hat{F}(k), \tag{2.3}$$

where $\hat{\gamma}$ denotes the Fourier transform of γ. Inverting equation (2.3) is the main idea behind Calderón's method. However, one can also seek to solve directly for the perturbation as follows. By the same argument, when $\gamma = 1$,

$$\int_{\partial\Omega}\phi_1\Lambda_1\phi_2 \mathrm{d}s(x) = -2\pi^2|k|^2\int_{\Omega}\exp\left[2\pi \mathrm{i}x\cdot k\right]\mathrm{d}x. \tag{2.4}$$

Subtracting this from equation (2.2) results in

$$\int_{\partial\Omega}\phi_1(\Lambda_\gamma - \Lambda_1)\phi_2 \mathrm{d}s(x) = -2\pi^2|k|^2\int_{\Omega}(\gamma-1)\exp\left[2\pi \mathrm{i}x\cdot k\right]\mathrm{d}x + \tilde{E}(k).$$

Denote

$$\mathcal{D}(k) \equiv \int_{\partial\Omega}\phi_1(\Lambda_\gamma - \Lambda_1)\phi_2 \mathrm{d}s(x).$$

Then,

$$\hat{\delta}(k) = -\frac{\mathcal{D}(k)}{2\pi^2|k|^2} + E(k), \tag{2.5}$$

and it is shown in [12] that $E(k)$ is bounded by $C\| \delta \|^2_{L^\infty}\exp\left[2\pi r|k|\right]$, where r is the radius of the smallest sphere containing Ω and C some constant. However, it is also shown in [12] that choosing α, $1 < \alpha < 2$, for $|k| \le \frac{2-\alpha}{2\pi r}\log\frac{1}{\| \delta \|_{L^\infty}}$,

$$|E(k)| \le C\| \delta \|^\alpha_\infty. \tag{2.6}$$

Now let η be a mollifier whose Fourier transform $\hat{\eta} \in C^\infty$, $\hat{\eta}(0) = 1$, and let $\eta_t(x) \equiv t^n\eta(tx)$, where t is a mollifying parameter. Then $\widehat{\eta_t}(k) = \hat{\eta}(k/t)$ acts as a low pass filter, and multiplying equation (2.5) by $\widehat{\eta_t}(k)$, we have,

$$\hat{\delta}(k)\hat{\eta}\left(\frac{k}{t}\right) = -\frac{\mathcal{D}(k)}{2\pi^2|k|^2}\hat{\eta}\left(\frac{k}{t}\right) + E(k)\hat{\eta}\left(\frac{k}{t}\right).$$

Taking the inverse Fourier transform,

$$(\delta * \eta_t)(x) = -\int_{\mathbb{R}^2} \frac{\mathcal{D}(k)}{2\pi^2|k|^2}\hat{\eta}\left(\frac{k}{t}\right) \exp\left[2\pi i x \cdot k\right] \mathrm{d}k + \rho(x),$$

where $*$ denotes the convolution, and ρ the error term, which is the term that depends on the data $\Lambda_\gamma - \Lambda_1$ nonlinearly. It was shown in [12] that $\rho(x)$ has a bound

$$|\rho(x)| \leq C\| \delta \|_{L^\infty}^{\alpha} \left[\log \frac{1}{\| \delta \|_{L^\infty}}\right]^2$$

which converges to zero as $\| \delta \|_{L^\infty}$ goes to zero. In the practical implementation, we also truncate $\mathcal{D}(k)$ to a region $|k| < R_1$ for some constant R_1. Therefore, we take

$$\delta_{R_1}^{\mathrm{app}}(x) \equiv -\int_{|k|<R_1} \frac{\mathcal{D}(k)}{2\pi^2|k|^2}\hat{\eta}\left(\frac{k}{t}\right) \exp\left[2\pi \mathrm{i} x \cdot k\right] \mathrm{d}k \tag{2.7}$$

as an approximation to $\delta(x)$. In this paper, we will call (2.7) *the first order Calderón's method.* We note that the reconstruction process

$$\Lambda_\gamma - \Lambda_1 \longrightarrow \mathcal{D}(k) \longrightarrow \delta_{R_1}^{\mathrm{app}}(x)$$

is linear and holds for real or complex-valued γ.

2.2.3 The D-bar method background

We now review the D-bar method based on the constructive global uniqueness proof by A. Nachman [60]. As in [60], now assume that $\gamma \in C^2(\Omega)$ is a real-valued conductivity bounded away from zero, and without loss of generality that $\gamma(x) \equiv 1$ for x in a neighborhood $\partial\Omega$. For consistency with Calderón's method, further assume that γ is of the form $\gamma = 1 + \delta$. Define the potential $q = \frac{\triangle\sqrt{\gamma}}{\sqrt{\gamma}}$, and make the change of variables $\tilde{u} = \sqrt{\gamma}u$. Then (2.1) is transformed to the Schrödinger equation

$$(-\triangle + q)\tilde{u} = 0 \quad \text{in } \Omega. \tag{2.8}$$

Smoothly extend $\gamma \equiv 1$ and $q \equiv 0$ outside Ω and consider (2.8) in the entire plane. Introduce a complex parameter $k = k_1 + \mathrm{i}k_2$ and identify it with $k = (k_1, k_2) \in \mathbb{R}^2$, depending on the context. The spatial variable $x = (x_1, x_2) \in \mathbb{R}^2$ is also identified as $x = x_1 + \mathrm{i}x_2$. Further introduce two harmonic functions $\mathrm{e}^{\mathrm{i}kx}$ and $\mathrm{e}^{\mathrm{i}\overline{k}\overline{x}}$ that satisfy (2.8) when $q = 0$. It is shown in [60] that there exist CGO solutions $\psi(x, k)$ to

$$(-\triangle + q)\psi(\cdot, k) = 0$$

satisfying the asymptotic condition

$$\mathrm{e}^{-\mathrm{i}kx}\psi(x, k) - 1 \in W^{1,\tilde{p}}(\mathbb{R}^2) \tag{2.9}$$

for any $2 < \tilde{p} < \infty$. Note that if $\gamma = const.$, so that $q \equiv 0$, then $\psi(x, k) = \mathrm{e}^{\mathrm{i}kx}$. Let

$$\mu(x, k) \equiv \mathrm{e}^{-\mathrm{i}kx}\psi(x, k),$$

and define the scattering transform $\mathbf{t}(k)$ of $q(x)$ by

$$\mathbf{t}(k) \equiv \int_{\mathbb{R}^2} \mathrm{e}^{\mathrm{i}\overline{k}\overline{x}} q(x)\psi(x, k)\mathrm{d}x,$$

or equivalently,

$$\mathbf{t}(k) := \int_{\mathbb{R}^2} e_k(x)q(x)\mu(x, k)\mathrm{d}x,$$

where

$$e_k(x) \equiv \exp\left[\mathrm{i}(kx + \overline{k}\overline{x})\right] = \exp\left[-\mathrm{i}(-2k_1, 2k_2) \cdot (x_1, x_2)\right].$$

The function μ satisfies

$$(-\triangle - 4\mathrm{i}k\overline{\partial})\mu(x,k) = -q(x)\mu(x,k). \tag{2.10}$$

Therefore, for a fundamental solution $g_k(x)$ satisfying

$$(-\triangle - 4\mathrm{i}k\overline{\partial})g_k(x) = \delta(x),$$

where $\delta(x)$ only in this line indicates the Dirac delta function, the function μ satisfies, with the asymptotic condition (2.9), the Lippmann-Schwinger-type integral equation

$$\mu = 1 - g_k * (q\mu). \tag{2.11}$$

Applying the $\overline{\partial}_k$ operator to (2.11) results in the $\overline{\partial}$ equation

$$\frac{\partial}{\partial \overline{k}}\mu(x,k) = \frac{1}{4\pi\overline{k}}\mathbf{t}(k)e_{-k}(x)\overline{\mu(x,k)}, \quad k \in \mathbb{C}\backslash 0, \quad x \in \mathbb{R}^2,$$

which is equivalent to the weakly singular Fredholm integral equation of the second kind

$$\mu(x,k) = 1 + \frac{1}{(2\pi)^2}\int_{\mathbb{R}^2} \frac{\mathbf{t}(k')}{(k-k')\overline{k'}}e_{-x}(k')\overline{\mu(x,k')}\mathrm{d}k_1'\mathrm{d}k_2'. \tag{2.12}$$

Taking the small k limit as $k \to 0$ in (2.10), and recalling that $q(x) = \frac{\triangle\sqrt{\gamma(x)}}{\sqrt{\gamma(x)}}$,

$$\triangle\mu(x,0) = \frac{\triangle\sqrt{\gamma(x)}}{\sqrt{\gamma(x)}}\mu(x,0). \tag{2.13}$$

It is a direct substitution to check that $\mu(x,0) = \sqrt{\gamma(x)}$ satisfies (2.13) and the asymptotic condition (2.9). Therefore, we can recover $\gamma(x)$ from (2.12) by

$$\gamma(x) = \mu(x,0)^2. \tag{2.14}$$

A key step in the D-bar method is to connect the data $\Lambda_\gamma - \Lambda_1$ to the scattering transform $\mathbf{t}(k)$ and to solve (2.12). This is done by first solving

$$\psi(x,k) = \mathrm{e}^{\mathrm{i}kx}\big|_{\partial\Omega} - \int_{\partial\Omega} G_k(\zeta - x)(\Lambda_\gamma - \Lambda_1)\psi(\zeta,k)\mathrm{d}s(\zeta), \tag{2.15}$$

where $G_k(x) = \mathrm{e}^{\mathrm{i}kx} g_k(x)$. The scattering transform $\mathbf{t}(k)$ is related to the data as, by [60],

$$\mathbf{t}(k) = \int_{\partial\Omega} \mathrm{e}^{\mathrm{i}\bar{k}\bar{x}}(\Lambda_\gamma - \Lambda_1)\psi(\cdot,k)\mathrm{d}s(x). \tag{2.16}$$

In the case of $\gamma \in L^\infty$, the existence and uniqueness of solutions to (2.12) and (2.15) is proven in [48]. However, (2.15) is very sensitive to noise in $\Lambda_\gamma - \Lambda_1$ and so are (2.16) and (2.12). In [68], approximating $\psi(x,k)$ by its asymptotic behavior $\mathrm{e}^{\mathrm{i}kx}$ is suggested and

$$\mathbf{t}^{\exp}(k) \equiv \int_{\partial\Omega} \mathrm{e}^{\mathrm{i}\bar{k}\bar{x}}(\Lambda_\gamma - \Lambda_1)\mathrm{e}^{\mathrm{i}kx}\mathrm{d}s(x) \tag{2.17}$$

is introduced as an approximation of (2.16). In terms of the integral equation (2.15), this approximation amounts to ignoring the scattering of the incident wave $\mathrm{e}^{\mathrm{i}kx}$ at the boundary $\partial\Omega$. Replacing $\psi(\zeta,k)$ on the right hand side of (2.15) by $\mathrm{e}^{\mathrm{i}k\zeta}$ can also be considered as a Born approximation. The approximation $\mathbf{t}^{\exp}$ was further studied with simulated noisy data $\Lambda_\gamma - \Lambda_1$ in [54]. While $\mathbf{t}^{\exp}(k)$ and (2.10) remain stable for large $|k|$ for simulated noise-free data, $\mathbf{t}^{\exp}(k)$ with noisy data blows up to infinity exponentially as $|k|$ gets large. This has been overcome by truncating $\mathbf{t}(k)$ to a bounded region $|k| < R_1$ for some R_1 constant [54]. Therefore, in the practical implementation, the integral equation (2.12) is solved in the region $|k| < R_1$.

2.3 Relationship between Calderón's method and the D-bar method and the second order Calderón's method

A connection between Calderón's method and the D-bar method was first shown in [46]. Based on [46], we provide explicit correction terms to Calderón's method and suggest a modified Calderón's method with one of the correction terms.

We first note the similarity of the CGO solutions that are used in both methods. Let $k = (k_1, k_2)$ and $a = (k_2, -k_1)$. We also identify $k = k_1 + ik_2$ and $a = k_2 - ik_1$, depending on the context. By simply changing the notation from vectors in $\mathbb{R}^2$ to complex variables,

$$\begin{aligned}\phi_1(x;k,a) &= e^{\pi(ik\cdot x - a\cdot x)} \\ &= e^{\pi(i(k_1,k_2)\cdot(x_1,x_2)-(k_2,-k_1)\cdot(x_1,x_2))} \\ &= e^{\pi(i(k_1x_1+k_2x_2)-k_2x_1+k_1x_2)} \\ &= e^{i\pi(k_1x_1+k_2x_2+i(k_2x_1-k_1x_2)} \\ &= e^{i\pi k\overline{x}},\end{aligned}$$

and similarly, $\phi_2(x;k,a) = e^{i\pi\overline{k}x}$. Therefore, the functions $\mathrm{e}^{\mathrm{i}\overline{kx}}, \mathrm{e}^{\mathrm{i}kx}$ in the D-bar method and $\phi_1,\ \phi_2$ are the same kind except for the π factor in the exponent and the fact that the variable k being complex conjugated. That is,

$$\mathcal{D}(k) = \int_{\partial\Omega} e^{i\pi k\overline{x}}(\Lambda_\gamma - \Lambda_1)e^{i\pi\overline{k}x}\mathrm{d}s(x) = \mathbf{t}^{\mathbf{exp}}(\pi\overline{k}). \tag{2.18}$$

Since $\mathcal{D}$ holds for complex-valued conductivities by (2.3), $\mathbf{t}^{\exp}$ is also well-defined for complex-valued conductivities. Now, from (2.5),

$$\hat{\delta}(k) = -\frac{1}{2\pi^2|k|^2}\mathbf{t}^{\exp}(\pi\overline{k}) + E(k). \tag{2.19}$$

By neglecting $E(k)$, multiplying a mollifier, taking the inverse Fourier transform, and then with a simple change of variables, we arrive at the same conclusion as in [46]. In [46], starting from (2.17), Calderón's method is re-derived with $\mathbf{t}^{\exp}(k)$ instead of $\mathcal{D}(k)$, and presented as

$$\delta^{\mathrm{app}}(x) \quad = \quad -\int_{\mathbb{R}^2} \frac{\mathbf{t}^{\exp}(k)}{2\pi^2|k|^2}\hat{\eta}(k/t)e_{-x}(k)\mathrm{d}k_1\mathrm{d}k_2, \tag{2.20}$$

and it is concluded that Calderón's method is a three-step linearized D-bar method. See section 6.1 of [46] for the full derivations. In the practical implementation, we truncate $\mathbf{t}^{\exp}(k)$ to a bounded region $|k|< R_1$ and denote the reconstructed perturbation by

$$\delta_{R_1}^{\mathrm{app}}(x) = -\int_{|k|<R_1} \frac{\mathbf{t}^{\exp}(k)}{2\pi^2|k|^2}\hat{\eta}(k/t)e_{-x}(k)\mathrm{d}k_1\mathrm{d}k_2, \tag{2.21}$$

which is equivalent to (2.7). Note that the truncation radius in this paper differs by the factor π from the truncation radius in other D-bar papers due to the relation (2.18). We further explicitly formulate the difference between Calderón's method and the D-bar method and connect them. Note that from (2.12), by simply putting $k=0$, (2.14) can be written formally as

$$\gamma(x) = 1 - \frac{1}{2\pi^2}\int_{\mathbb{R}^2} \frac{\mathbf{t}(k)}{|k|^2}e_{-x}(k)\overline{\mu(x,k)}\mathrm{d}k_1\mathrm{d}k_2 + \left\{\frac{1}{(2\pi)^2}\int_{\mathbb{R}^2} \frac{\mathbf{t}(k)}{|k|^2}e_{-x}(k)\overline{\mu(x,k)}\mathrm{d}k_1\mathrm{d}k_2\right\}^2,$$

or equivalently,

$$\delta(x) = -\frac{1}{2\pi^2}\int_{\mathbb{R}^2} \frac{\mathbf{t}(k)}{|k|^2}e_{-x}(k)\overline{\mu(x,k)}\mathrm{d}k_1\mathrm{d}k_2 + \left\{\frac{1}{(2\pi)^2}\int_{\mathbb{R}^2} \frac{\mathbf{t}(k)}{|k|^2}e_{-x}(k)\overline{\mu(x,k)}\mathrm{d}k_1\mathrm{d}k_2\right\}^2. \tag{2.22}$$

Note that this line is from the D-bar method while (2.21) is Calderón's method. Now we explicitly provide the connection between them. For $\|q(x)\|_\infty$ small, let $\tilde{\psi}(x,k)$ be a small perturbation from $\mathrm{e}^{\mathrm{i}kx}$ and write

$$\psi(x,k) = \mathrm{e}^{\mathrm{i}kx} + \tilde{\psi}(x,k).$$

Then $\mu(x,k) \equiv 1 + \tilde{\mu}(x,k)$, and

$$\begin{aligned}
\mathbf{t}(k) &= \int_{\partial\Omega} \mathrm{e}^{\mathrm{i}\bar{k}\bar{x}}(\Lambda_\gamma - \Lambda_1)\psi(x,k)\mathrm{d}s(x) \\
&= \int_{\partial\Omega} \mathrm{e}^{\mathrm{i}\bar{k}\bar{x}}(\Lambda_\gamma - \Lambda_1)(\mathrm{e}^{\mathrm{i}kx} + \tilde{\psi}(x,k))\mathrm{d}s(x) \\
&= \mathbf{t}^{\exp}(k) + \int_{\partial\Omega} \mathrm{e}^{\mathrm{i}\bar{k}\bar{x}}(\Lambda_\gamma - \Lambda_1)\tilde{\psi}(x,k)\mathrm{d}s(x) \\
&= \mathbf{t}^{\exp}(k) + \tilde{\mathbf{t}}(k),
\end{aligned}$$

where $\tilde{\mathbf{t}}(k)$ and $\tilde{\mu}(x,k)$ are also small perturbations if $\|q(x)\|_\infty$ is small. We derive the second order Calderón's method as follows. Recall, the definition of the norm on $W^{1,\tilde{p}}$:

$$\|u\|_{W^{1,\tilde{p}}} = \|u\|_{L^{\tilde{p}}} + \|\nabla u\|_{L^{\tilde{p}}} \tag{2.23}$$

Lemma 4.1 in [59] states the following.

Theorem 1. *Fix* $p \in (1,2), k \in \mathbb{C}\backslash\{0\}$, *and* $q_0 \in L^p(\mathbb{R}^2)$. *Let* $\frac{1}{\tilde{p}} + \frac{1}{p} = \frac{1}{2}$. *Suppose that*

$$R(q_0) := (I - S_k(q_0))^{-1}$$

exists as a bounded operator from $W^{1,\tilde{p}}(\mathbb{R}^2)$ *to itself. There is a number* $r > 0$ *and a constant* $c(p,k,q_0)$ *so that for all* $q \in L^p(\mathbb{R}^2)$ *with* $||q_0 - q||_p \leq r$, *the estimate*

$$||\mu(\cdot,k,q) - \mu(\cdot,k,q_0)||_{W^{1,\tilde{p}}} \leq c(p,k,q_0)||q - q_0||_p \tag{2.24}$$

holds.

Let $K_R = \{k \in \mathbb{C} : |k| \leq R_1\}$. Note that in Theorem 1, $\tilde{p} \in (2,\infty)$. For $\gamma = 1, q_0 = 0$ and $\mu(\cdot,k,q_0) = 1$, the theorem implies

$$||\tilde{\mu}(\cdot,k,q)||_{W^{1,\tilde{p}}(K_R)} \leq c(p,R)||q||_p \leq c'(p,R,\Omega)||q||_\infty. \tag{2.25}$$

Corollary 1. *Under the assumptions of Theorem 1,*

$$\|\tilde{\psi}(\cdot,k)\|_{W^{1,\tilde{p}}(K_R)} \leq C(p,R,\Omega)||q||_\infty.$$

Proof:

$$\begin{aligned}
\|\tilde{\psi}(\cdot,k)\|_{W^{1,\tilde{p}}(K_R)} &= ||e^{ikx}\tilde{\mu}(\cdot,k)||_{W^{1,\tilde{p}}(K_R)} \\
&= \left\{\int_{K_R}|e^{ikx}\tilde{\mu}(x,k)|^{\tilde{p}}dk\right\}^{1/\tilde{p}} + \left\{\int_{K_R}|\nabla(e^{ikx}\tilde{\mu}(x,k)|^{\tilde{p}})dk\right\}^{1/\tilde{p}} \\
&\leq C\|\tilde{\mu}(\cdot,k)||_{L^{\tilde{p}}(K_R)} + \left\{\int_{K_R}|\nabla(e^{ikx})\tilde{\mu}(x,k) + e^{ikx}\nabla\tilde{\mu}(x,k)|^{\tilde{p}})dk\right\}^{1/\tilde{p}} \\
&\leq C\|\tilde{\mu}(\cdot,k)||_{L^{\tilde{p}}(K_R)} + \tilde{C}\|\tilde{\mu}(\cdot,k)||_{L^{\tilde{p}}(K_R)} + C\|\nabla\tilde{\mu}(\cdot,k)||_{L^{\tilde{p}}(K_R)} \\
&= C\|\tilde{\mu}(\cdot,k,q)||_{W^{1,\tilde{p}}(K_R)} + \tilde{C}\|\tilde{\mu}(\cdot,k)||_{L^{\tilde{p}}(K_R)} \\
&= C_1\|\tilde{\mu}(\cdot,k,q)||_{W^{1,\tilde{p}}(K_R)} \\
&\leq C_2(p,R)||q||_p \\
&\leq C_2(p,R)(\text{area of } \Omega)||q||_\infty.
\end{aligned}$$

where the third inequality follows from Minkowski's inequality and the fifth inequality from (2.25).

□

Corollary 2. *Under the assumptions of Theorem 1,* $\tilde{\mathbf{t}}(k) \in W^{1,\tilde{p}}(K_R)$ *and*

$$\|\tilde{\mathbf{t}}(k)\|_{W^{1,\tilde{p}}(K_R)} \leq C(p,R,\Omega)\|q\|_\infty$$

Proof:

$$\begin{aligned}
\|\tilde{\mathbf{t}}(k)\|_{W^{1,\tilde{p}}(K_R)} &= \left\{\int_{K_R}|e^{i\bar{k}\bar{x}}q(x)\tilde{\psi}(x,k)|^{\tilde{p}}dk\right\}^{1/\tilde{p}} + \left\{\int_{K_R}|\nabla(e^{i\bar{k}\bar{x}}q(x)\tilde{\psi}(x,k))|^{\tilde{p}}dk\right\}^{1/\tilde{p}} \\
&\leq C\|q\|_\infty\|\tilde{\psi}(x,k))\|_{L^{\tilde{p}}(K_R)} + \|q\|_\infty\left\{\int_{K_R}|\nabla(e^{i\bar{k}\bar{x}}\tilde{\psi}(x,k))|^{\tilde{p}}dk\right\}^{1/\tilde{p}} \\
&\leq \|q\|_\infty(C\|\tilde{\psi}(\cdot,k,q)||_{W^{1,\tilde{p}}(K_R)} + \tilde{C}\|\tilde{\psi}(\cdot,k,q)||_{L^{\tilde{p}}(K_R)})
\end{aligned}$$

$$
\begin{aligned}
&\leq C'\|q\|_\infty \|\tilde{\psi}(\cdot,k,q)\|_{W^{1,\tilde{p}}(K_R)} \\
&\leq C(p,R,\Omega)\|q\|_\infty,
\end{aligned}
$$

where the second inequality follows from Minkowski's inequality and the remainder by the analogous argument as in Corollary 1. □

Then, expanding the integrands in (2.22) and folding out the square in the second term, one sees that compared to (2.20), (2.22) has three more first order terms and 16 more second order terms which depend on the data $\Lambda_\gamma - \Lambda_1$ nonlinearly. All integrals in practice are over K_R, and

$$
\begin{aligned}
\delta(x) &= -\int_{K_R} \frac{\mathbf{t}^{\exp}(k)+\tilde{\mathbf{t}}(k)}{2\pi^2|k|^2} e_{-x}(k)\overline{1+\tilde{\mu}(x,k)}\mathrm{d}k \\
&+ \left\{\frac{1}{(2\pi)^2}\int_{K_R} \frac{\mathbf{t}^{\exp}(k)+\tilde{\mathbf{t}}(k)}{|k|^2} e_{-x}(k)\overline{1+\tilde{\mu}(x,k)}\mathrm{d}k\right\}^2 \\
&= -\int_{K_R} \frac{\mathbf{t}^{\exp}(k)}{2\pi^2|k|^2} e_{-x}(k)\mathrm{d}k - \int_{K_R} \frac{\mathbf{t}^{\exp}(k)}{2\pi^2|k|^2} e_{-x}(k)\overline{\tilde{\mu}(x,k)}\mathrm{d}k \qquad (2.26)\\
&- \int_{K_R} \frac{\tilde{\mathbf{t}}(k)}{2\pi^2|k|^2} e_{-x}(k)\mathrm{d}k - \int_{K_R} \frac{\tilde{\mathbf{t}}(k)}{2\pi^2|k|^2} e_{-x}(k)\overline{\tilde{\mu}(x,k)}\mathrm{d}k \qquad (2.27)\\
&+ \left\{\frac{1}{(2\pi)^2}\int_{K_R} \frac{\mathbf{t}^{\exp}(k)}{|k|^2} e_{-x}(k)\mathrm{d}k\right\}^2 + \left\{\frac{1}{(2\pi)^2}\int_{K_R} \frac{\mathbf{t}^{\exp}(k)}{|k|^2} e_{-x}(k)\overline{\tilde{\mu}(x,k)}\mathrm{d}k\right\}^2 \qquad (2.28)\\
&+ \left\{\frac{1}{(2\pi)^2}\int_{K_R} \frac{\tilde{\mathbf{t}}(k)}{|k|^2} e_{-x}(k)\mathrm{d}k\right\}^2 + \left\{\frac{1}{(2\pi)^2}\int_{K_R} \frac{\tilde{\mathbf{t}}(k)}{|k|^2} e_{-x}(k)\overline{\tilde{\mu}(x,k)}\mathrm{d}k\right\}^2 \\
&+ 2\left\{\frac{1}{(2\pi)^2}\int_{K_R} \frac{\mathbf{t}^{\exp}(k)}{|k|^2} e_{-x}(k)\mathrm{d}k\right\}\left\{\frac{1}{(2\pi)^2}\int_{K_R} \frac{\mathbf{t}^{\exp}(k)}{|k|^2} e_{-x}(k)\overline{\tilde{\mu}(x,k)}\mathrm{d}k\right\} \\
&+ 2\left\{\frac{1}{(2\pi)^2}\int_{K_R} \frac{\mathbf{t}^{\exp}(k)}{|k|^2} e_{-x}(k)\mathrm{d}k\right\}\left\{\frac{1}{(2\pi)^2}\int_{K_R} \frac{\tilde{\mathbf{t}}(k)}{|k|^2} e_{-x}(k)\mathrm{d}k\right\} \\
&+ 2\left\{\frac{1}{(2\pi)^2}\int_{K_R} \frac{\mathbf{t}^{\exp}(k)}{|k|^2} e_{-x}(k)\mathrm{d}k\right\}\left\{\frac{1}{(2\pi)^2}\int_{K_R} \frac{\tilde{\mathbf{t}}(k)}{|k|^2} e_{-x}(k)\overline{\tilde{\mu}(x,k)}\mathrm{d}k\right\} \\
&+ 2\left\{\frac{1}{(2\pi)^2}\int_{K_R} \frac{\mathbf{t}^{\exp}(k)}{|k|^2} e_{-x}(k)\overline{\tilde{\mu}(x,k)}\mathrm{d}k\right\}\left\{\frac{1}{(2\pi)^2}\int_{K_R} \frac{\tilde{\mathbf{t}}(k)}{|k|^2} e_{-x}(k)\mathrm{d}k\right\} \\
&+ 2\left\{\frac{1}{(2\pi)^2}\int_{K_R} \frac{\mathbf{t}^{\exp}(k)}{|k|^2} e_{-x}(k)\overline{\tilde{\mu}(x,k)}\mathrm{d}k\right\}\left\{\frac{1}{(2\pi)^2}\int_{K_R} \frac{\tilde{\mathbf{t}}(k)}{|k|^2} e_{-x}(k)\overline{\tilde{\mu}(x,k)}\mathrm{d}k\right\} \\
&+ 2\left\{\frac{1}{(2\pi)^2}\int_{K_R} \frac{\tilde{\mathbf{t}}(k)}{|k|^2} e_{-x}(k)\mathrm{d}k\right\}\left\{\frac{1}{(2\pi)^2}\int_{K_R} \frac{\tilde{\mathbf{t}}(k)}{|k|^2} e_{-x}(k)\overline{\tilde{\mu}(x,k)}\mathrm{d}k\right\}. \qquad (2.29)
\end{aligned}
$$

Assume $\|q\|_\infty$ is sufficiently small so that $||\tilde{\mu}(\cdot,k,q)||_{W^{1,\tilde{p}}(K_R)} \leq 1$ and $\|\tilde{\mathbf{t}}(k)\|_{W^{1,\tilde{p}}(K_R)} \leq \|\mathbf{t}^{\exp}(k)\|_{W^{1,\tilde{p}}(K_R)}$. Note [54] that $|\mathbf{t}^{\exp}(k)| \leq C|k|^2$ for $k \in K_R$ and $|e_{-x}(k)| = 1$. Then $\mathbf{t}^{\exp}(k)/|k|^2 \in L^r(K_R),\ r = 2-\varepsilon$, where here ε is a small value less than 1, and r is the Hölder conjugate of $\tilde{p}$. Thus, by Hölder's inequality, the following shows that the first term in (2.26) dominates the second term:

$$\begin{aligned}
\left|\int_{K_R} \frac{\mathbf{t}^{\exp}(k)}{2\pi^2|k|^2} e_{-x}(k)\overline{\tilde{\mu}(x,k)}\mathrm{d}k\right| &\leq \left\{\int_{K_R}\left|\frac{\mathbf{t}^{\exp}(k)}{2\pi^2|k|^2}\right|^r \mathrm{d}k\right\}^{1/r}\left\{\int_{K_R}\left|\overline{\tilde{\mu}(x,k)}\right|^{\tilde{p}}\mathrm{d}k\right\}^{1/\tilde{p}} \\
&\leq ||\tilde{\mu}(\cdot,k,q)||_{W^{1,\tilde{p}}(K_R)}\left\{\int_{K_R}\left|\frac{\mathbf{t}^{\exp}(k)}{2\pi^2|k|^2}\right|^r \mathrm{d}k\right\}^{1/r} \\
&\leq \left\{\int_{K_R}\left|\frac{\mathbf{t}^{\exp}(k)}{2\pi^2|k|^2}\right|^r \mathrm{d}k\right\}^{1/r}.
\end{aligned}$$

Also since $\|\tilde{\mathbf{t}}(k)\|_{W^{1,\tilde{p}}(K_R)} \leq \|\mathbf{t}^{\exp}(k)\|_{W^{1,\tilde{p}}(K_R)}$, the first term in (2.27) is smaller than the first term in (2.26), and likewise, the second term in (2.27) is smaller than the first term in (2.26). Thus, among the first order terms in the expansion of $\delta(x)$, the first term is dominant. Analogous arguments show that the first term in (2.28) is larger than all subsequent second order terms.

Therefore, we suggest a modified Calderón's method by adding the known second order term and define

$$\delta_{R_1}^{\text{app,sec}}(x) = \delta_{R_1}^{\text{app}}(x) + \left(\beta\delta_{R_1}^{\text{app}}(x)\right)^2, \tag{2.30}$$

where β is a weighting parameter for the second order term. One can change the value β to adjust the impact of the second order term. For the results in Figure 2.3, we chose $\beta = 0.5$, and for all the other examples we chose $\beta = 0.7$. We will call (2.30) *the second order Calderón's method*, and compare the reconstructions with (2.30) to the first order Calderón's method (2.7). Since we use (2.7) for the first order Calderon's method, from the equation (2.18), the truncation radius $R_1 = 1.5$, for example, in our paper is equivalent to the truncation radius $1.5{\cdot}\pi \approx 4.712$ for the D-bar method with $\mathbf{t}^{\mathbf{exp}}(k)$ in other papers. Note that since $\delta_{R_1}^{\text{app}}(x)$ is well-defined for complex-valued conductivities, the second order method can be applied to complex-valued data arising from such conductivities, even though the derivation of the method is based on the real-valued case.

In Figure 2.2, we illustrate the effect of the second order term in the second order Calderón's method on reconstructions for case (i). Figure 2.2 shows the absolute images for the case (i), where (A) and (C) depict the image with the first order Calderón's method, and (B) and (D) depict the images with the second order Calderón's method, with the truncation radius $R_1 = 1.125$ and $R_1 = 1.35$, respectively, with no prior inclusion. Compared to (A) and (C), the organs are more sharper and the artifacts near the boundary are reduced in (B) and (D). To quantify the quality of the reconstructions, we use Structural Similarity (SSIM) index. See [82]. The resultant SSIM value is a decimal number between -1 and 1. SSIM index is 1 when an image is identical to the reference image, and 0 when an image has no similarity to the reference image. We use Figure 2.1 (D) as the reference image for SSIM values given below each reconstruction. SSIM values support our claim too. This kind of improvement was observed in all examples to varying degrees. In order to test the validity of the second order Calderon's method for complex valued admittivity, we simulated data with complex valued admittivity thoracic example, Figure 2.3. To generate the data, we solved an associated forward problem by the Finite Element Method (FEM). The admittivity of the heart, lungs, and the background are $2 + i\omega(0.88 \times 10^{-6})$, $0.5 + i\omega(0.22 \times 10^{-6})$ and $1 + i\omega(0.55 \times 10^{-6})$, respectively, where $\omega = 2\pi \times 28.8$. The results show that the second order Calderón's method improves the reconstruction. Therefore, in the results section, we only present the reconstructions by the second order Calderón's method, whether or not those are absolute images, difference images, images without a prior or images with a prior.

2.3.1 Computational considerations

The results shown in this work are on experimental data and so the assumption of Calderón's method that the conductivity distribution is a small perturbation from the background conductivity 1 is violated by our phantoms. This is overcome by rescaling as follows in an approach also taken in [39]. Let $\gamma(x) = \gamma_0 + \delta(x)$, where $\gamma_0 > 0$ is the background constant conductivity and $\delta(x)$ is

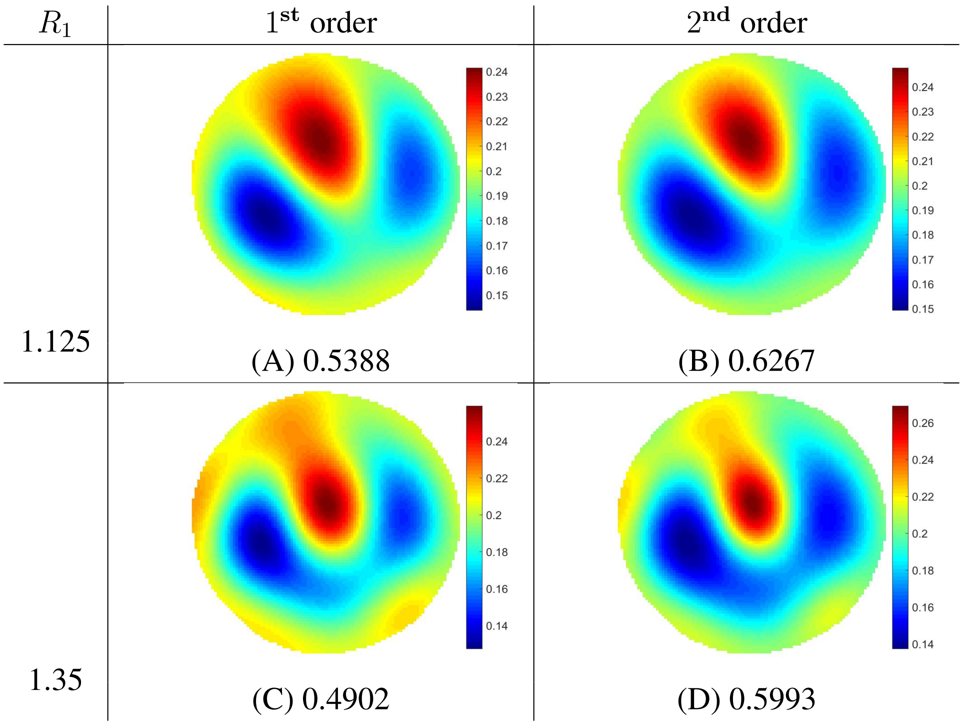

Figure 2.2: Absolute images for Case (i) with $R_1 = 1.125$ for (A) and (B), $R_1 = 1.35$ for (C) and (D). (A) and (C) are the images by the 1^{st} order Calderón's method. (B) and (D) are the images by the 2^{nd} order Calderón's method. The values that are provided are the SSIM measures.

the perturbation from γ_0. Scale γ by γ_0 and denote

$$\tilde{\gamma} = \frac{\gamma}{\gamma_0} = 1 + \frac{\delta}{\gamma_0}.$$

Since $\Lambda_{c\gamma} = c\Lambda_\gamma$ for c constant, $\Lambda_{\tilde{\gamma}} = \frac{1}{\gamma_0}\Lambda_\gamma$. We use this map to compute the scaled perturbation $\tilde{\delta} = \frac{\delta}{\gamma_0}$. Once we reconstruct $\tilde{\delta}$, we obtain $\delta = \gamma_0\tilde{\delta}$ and γ. An approximation of γ_0 was obtained by first reconstructing $\gamma(x)$ without any scaling of the DN map, and then choosing an appropriate value in the region of background in the images. In the following lines, we simply denote $\Lambda_{\tilde{\gamma}}$ by Λ_γ for the simplicity of the notation.

Most of the images in this paper are *absolute images*. That is, they are computed using only one experimental data set, without an experimental reference. *Difference images* show the conductivity change from a reference image, which in this paper is the homogeneous tank containing only saline.

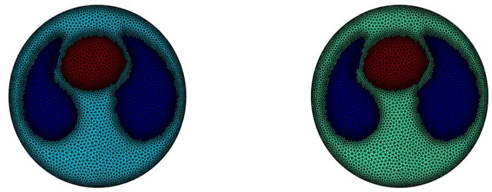

(A) Real part (B) Imaginary part

R_1	real part		imaginary part	
	1^{st} order	2^{st} order	1^{st} order	2^{st} order
1.125	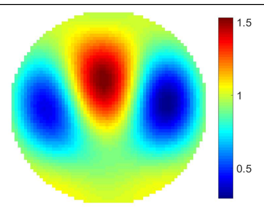 0.65612	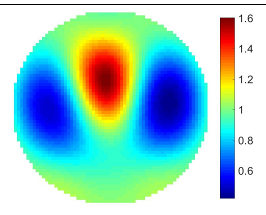 0.69923	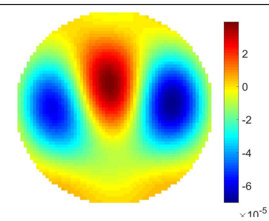 0.65831	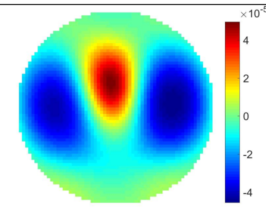 0.7076
1.35	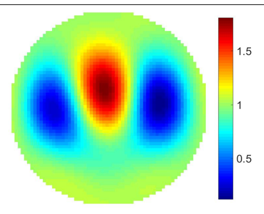 0.66664	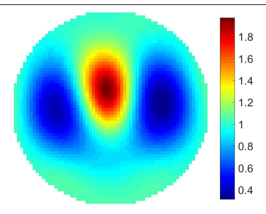 0.71949	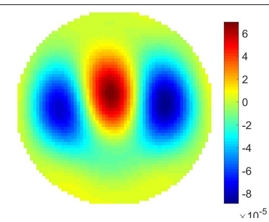 0.66986	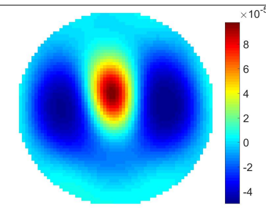 0.70162
1.575	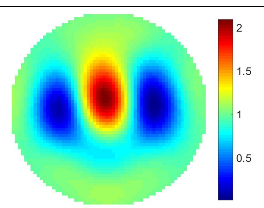 0.68402	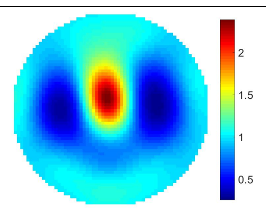 0.71773	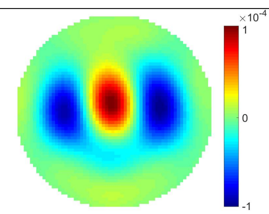 0.68475	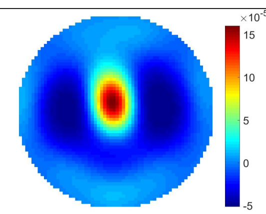 0.6934

Figure 2.3: The high contrast complex valued admittivity example where the admittivity of the heart, lungs, and the background are $2 + i\omega(0.88 \times 10^{-6})$, $0.5 + i\omega(0.22 \times 10^{-6})$ and $1 + i\omega(0.55 \times 10^{-6})$, respectively, where $\omega = 2\pi \times 28.8$. (A) is the real part ground truth, (B) is the imaginary part ground truth. R_1 is $1.125, 1.35$ and 1.575 from the top row to the bottom row. 1^{st} column is the real part of the first order reconstruction. 2^{nd} column is the real part of the second order reconstruction. 3^{rd} column is the imaginary part of the first order reconstruction. 4^{th} column is the imaginary part of the second order reconstruction. The values that are provided are the SSIM measures.

For the difference images, $\mathcal{D}(k)$ is replaced by $\mathcal{D}_{\text{dif}}$ defined by

$$\mathcal{D}_{\text{dif}}(k) \equiv \int_{\partial\Omega} \phi_1(\Lambda_\gamma - \Lambda_{ref})\phi_2 \mathrm{d}s(x), \tag{2.31}$$

where Λ_{ref} is the DN map computed from the reference data.

For practical computation of the absolute images, first write

$$\mathcal{D}(k) = \int_{\partial\Omega} \phi_1(\Lambda_\gamma - \Lambda_1)\phi_2 \mathrm{d}s(x) = \int_{\partial\Omega} \phi_1\Lambda_\gamma\phi_2 \mathrm{d}s(x) - \int_{\partial\Omega} \phi_1\Lambda_1\phi_2 \mathrm{d}s(x). \tag{2.32}$$

Now, let $x|_{\partial\Omega} = Re^{i\theta}$, where R is the radius of the tank. Then, by using the Taylor expansion of the exponential function, we get the Fourier type expansion of ϕ_1, ϕ_2 as

$$\phi_1 = e^{i\pi k\overline{x}} = \sum_{m=0}^{\infty} a_m(k)e^{-im\theta}, \;\; \phi_2 = e^{i\pi\overline{k}x} = \sum_{n=0}^{\infty} b_n(k)e^{in\theta},$$

where $a_m(k) = \frac{(i\pi kR)^m}{m!}$ and $b_n(k) = \frac{(i\pi\overline{k}R)^n}{n!}$. Let L be the number of electrodes, $\theta_l = \frac{2\pi l}{L}$ be the angle of the center of the l^{th} electrode, and let m^{th} trigonometric current pattern on l^{th} electrode be

$$T_l^m = \begin{cases} M\cos m\theta_l, & m = 1, \ldots, \frac{L}{2} - 1, \\ M\cos \pi l, & m = \frac{L}{2}, \\ M\sin((m - L/2)\theta_l), & m = \frac{L}{2} + 1, \ldots, L - 1, \end{cases}$$

where M is the amplitude of the current pattern, and let the normalized current pattern $t^m = \frac{T^m}{||T^m||_{L^2}}$. Define an inner product $(u(\cdot), w(\cdot))_{L^2} = \sum_{l=1}^{L} \overline{u(\theta_l)}w(\theta_l)$. Let $\mathbf{L}$ be the discretized DN map with entries $\mathbf{L}_{m,n} = \left(t_l^m, \left(\frac{R_\gamma}{A}\right)^{-1} t_l^n\right)_{L^2}$. We model the current density j on the boundary by the ave-gab model as

$$j^m(x) = \begin{cases} \frac{T_l^m}{A_l}, & x \in e_l, \\ 0, & x \notin e_l, \end{cases}$$

where e_l denotes the l^{th} electrode. Then,

$$
\begin{aligned}
&\int_{\partial\Omega} \phi_1 \Lambda_\gamma \phi_2 \mathrm{d}s(x) \\
&\approx R \sum_{m=1}^{L-1} \sum_{n=1}^{L-1} a_m b_n \int_0^{2\pi} e^{-im\theta} \Lambda_\gamma e^{in\theta} \mathrm{d}\theta, \\
&= R \sum_{m=1}^{L-1} \sum_{n=1}^{L-1} a_m b_n \int_0^{2\pi} (\cos m\theta - i \sin m\theta) \Lambda_\gamma (\cos n\theta + i \sin n\theta) \mathrm{d}\theta
\end{aligned}
$$

$$
\begin{aligned}
&= \frac{R\Delta\theta}{A} \sum_{m=1}^{L-1} \sum_{n=1}^{L-1} a_m b_n \left\{ \left(\cos m\cdot, \left(\frac{R_\gamma}{A} \right)^{-1} \cos n\cdot \right)_{L^2} + i \left(\cos m\cdot, \left(\frac{R_\gamma}{A} \right)^{-1} \sin n\cdot \right)_{L^2} \right. \\
&\left. - i \left(\sin m\cdot, \left(\frac{R_\gamma}{A} \right)^{-1} \cos n\cdot \right)_{L^2} + \left(\sin m\cdot, \left(\frac{R_\gamma}{A} \right)^{-1} \sin n\cdot \right)_{L^2} \right\} \\
&= \frac{R\Delta\theta}{A} \left\{ \sum_{m=1}^{L/2} \sum_{n=1}^{L/2} a_m b_n \left(\mathbf{L}_{m,n} + \mathbf{L}_{\frac{L}{2}+m,\frac{L}{2}+n} + i \left(\mathbf{L}_{m,\frac{L}{2}+n} - \mathbf{L}_{\frac{L}{2}+m,n} \right) \right) \right. \\
&+ \sqrt{2} \sum_{n=1}^{L/2-1} a_{\frac{L}{2}} b_n \left(\mathbf{L}_{\frac{L}{2},n} + i \mathbf{L}_{\frac{L}{2},\frac{L}{2}+n} \right) + \sqrt{2} \sum_{m=1}^{L/2-1} a_m b_{\frac{L}{2}} \left(\mathbf{L}_{m,\frac{L}{2}} - i \mathbf{L}_{\frac{L}{2}+m,\frac{L}{2}} \right) \\
&\left. + 2(-1)^{\frac{L}{2}} a_{\frac{L}{2}} b_{\frac{L}{2}} \mathbf{L}_{\frac{L}{2},\frac{L}{2}} \right\}.
\end{aligned}
$$

Here $\Delta\theta = \frac{2\pi}{L}$ is the angle between the center of electrodes. For the difference image, $\int_{\partial\Omega} \phi_1 \Lambda_{ref} \phi_2 \mathrm{d}s(x)$ is computed by the same way as above. On the other hand, from (2.4), $\int_{\partial\Omega} \phi_1 \Lambda_1 \phi_2 \mathrm{d}s(x) = -2\pi^2 |k|^2 \int_\Omega e^{2\pi \mathrm{i} x \cdot k} \mathrm{d}x$, and we compute the integral $\int_\Omega e^{2\pi \mathrm{i} x \cdot k} \mathrm{d}x$ by using a quadrature rule. Note that this differs computationally from the methods of [8, 56–58] where γ is approximated by computing the inverse Fourier transform of $\hat{F}(k)$ from (2.3). The reason why we include this second term, while one can simply ignore it and reconstruct γ directly from the first term only (which is $\hat{F}(k)$), is to compensate for the artifact along the boundary caused by the Gibbs phenomena. This method improves the absolute images significantly, as illustrated in Figure 2.4 on the first order Calderón's method.

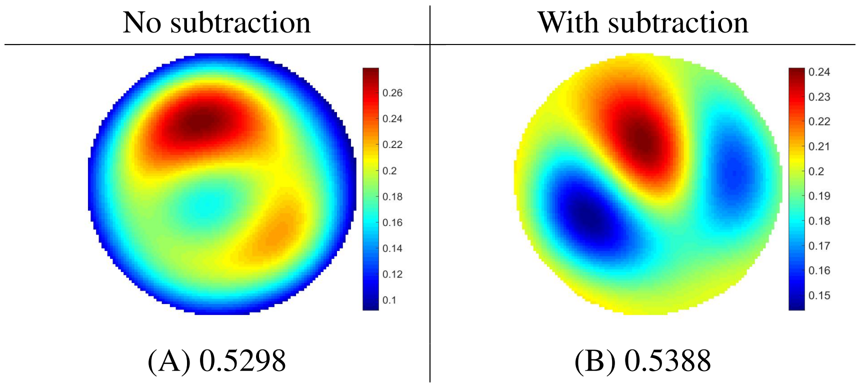

Figure 2.4: The absolute images for Case (i) with $R_1 = 1.125$. Image (A) is the reconstruction without subtracting the synthesized homogeneous term. Image (B) is the reconstruction with subtracting the synthesized homogeneous term. The values that are provided are the SSIM measures.

Figure 2.4 illustrates the absolute images for Case (i). (A) is the images computed from $\hat{F}(k)$ and (B) is the images with the subtraction of the synthesized homogeneous term. The truncation radius is $R_1 = 1.125$ for both images. As seen in Figure 2.4, the subtraction of the synthesized homogeneous term reduces the artifact along the boundary and therefore gives a better reconstruction.

2.4 Calderón's method with a spatial prior

We introduce a method of inclusion of *a priori* information to the first and second order Calderón's methods in the same spirit as [4] for the D-bar method. We assume that we know the approximate location of the inhomogeneous inclusions in Ω and approximate constant conductivity for each inclusion. We denote this *a priori* information by $\delta_{\text{pr}}(x)$ of which we will make use as follows. Denote $\hat{H}(k) = -\frac{1}{2\pi^2|k|^2}\mathcal{D}(k)\hat{\eta}\left(\frac{k}{t}\right)$ and define

$$\hat{H}_{R_1,R_2}(k) := \begin{cases} \hat{H}(k), & |k| \leq R_1, \\ \hat{\delta}_{\text{pr}}(k)\hat{\eta}(k/t), & R_1 < |k| \leq R_2, \\ 0, & |k| > R_2, \end{cases} \tag{2.33}$$

by appending $\hat{\delta}_{\rm pr}(k)\hat{\eta}(k/t)$ to the outer region of $|k|< R_1$ and inside of $|k|= R_2$ for some R_1 and R_2 . Since $\hat{\delta}_{\rm pr}(k)\hat{\eta}(k/t)$ is numerically stable, and it decreases to zero as $|k|$ tends to infinity, the outer truncation radius R_2 can be far bigger than R_1, giving more weight to the prior as R_2 increases or as R_1 decreases. Therefore, by taking the inverse Fourier transform of (2.33), we define

$$\delta^{\rm app}_{R_1,R_2}(x) = \mathcal{F}^{-1}\left(\hat{H}_{R_1,R_2}(k)\right)(x).$$

Since the inverse Fourier transform is a linear operation, this can be written as

$$\delta^{\rm app}_{R_1,R_2}(x) = \delta^{\rm app}_{R_1}(x) + \int_{R_1<|k|<R_2} \hat{\delta}_{\rm pr}(k)\hat{\eta}(k/t)e^{2\pi i k\cdot x}{\rm d}k. \tag{2.34}$$

Therefore, we can think of $\delta^{\rm app}_{R_1,R_2}(x)$ as the Calderóns method with a high pass filtered prior. We call (2.34) *the first order Calderon's method with a prior*. We apply this idea to (2.30) also and define

$$\delta^{\rm app,sec}_{R_1,R_2}(x) = \delta^{\rm app,sec}_{R_1}(x) + \int_{R_1<|k|<R_2} \hat{\delta}_{\rm pr}(k)\hat{\eta}(k/t)e^{2\pi i k\cdot x}{\rm d}k,$$

and call it *the second order Calderon's method with a prior*.

2.5 Experimental results and discussion

2.5.1 Cases (i) and (ii)

The experimental tank data for Cases (i) and (ii) were also used in [5], and are included here for the purpose of comparison with the D-bar method. It should be noted that the results in [5] are difference images, and here we include both difference and absolute images. The data was collected using the ACE1 EIT system at Colorado State University [52] on a circular tank with diameter 30 cm. The electrodes were 2.54 cm wide, and the level of saline bath was 1 cm. Adjacent current patterns were applied at 125 kHz with amplitude 3.3 mA. The phantoms are made of agar with a “heart" with conductivity 0.238 S/m, and right and left “lungs” with conductivity 0.136 S/m, and a saline bath of conductivity 0.190 S/m. Case (i) includes a copper pipe 1.6 cm in diameter inserted in the right lower lung region, and Case (ii) is the same agar targets with a PVC pipe 2.2 cm in diameter inserted in the same place as in Case (i).

Spatial priors without the pipes were constructed and used in the algorithm. To construct a prior conductivity $\gamma_{\rm pr}$, we open the photo of Case (i) in Matlab, click points along the boundary of the heart and lungs to generate boundary data, assign approximate conductivity values to each organ and apply a mollification by using convolution to have a smooth prior. Since we never know the accurate conductivity distribution in practical applications, we assign rather incorrect values for each organ. We used a prior with conductivity values 0.323, 0.190, 0.123, and 0.123 for the heart, background, left lung, and right lung, respectively.

2.5.2 Results and discussion for Cases (i) and (ii)

The absolute and difference images computed by the second order Calderón's method with and without a prior for Cases (i) and (ii) are found in Figures 2.5 and 2.6. The first column shows the absolute images without a prior, the second column shows the absolute images with a prior, the third column shows the difference images without a prior, and the last column shows the difference images with a prior. It is important to note that the prior does not include the pipes in the lung, mimicking the case of an unknown pathology in the lung. The inner truncation radius R_1 for each row is $1.125, 1.35$, and 1.575 from the top to the bottom row, and for the mollification function $\hat{\eta}(k/t)$ in (2.33), we used $\exp(-\pi|k|^2/t)$, where t is $500, 50$, and 5 for each row. As we increased the truncation radius R_1, we also increased the degree of the mollification which results in more suppression on $\hat{H}(k)$ for high frequency $|k|$. Otherwise, $\hat{H}(k)$ blows up very quickly as the truncation radius increases.

The outer truncation radius R_2 is 3 for all reconstructions. Because we fixed R_2, within which almost all of the practical information is included, a larger R_1 means that relatively more information from the measurement data is used and the influence of the prior is smaller. Therefore, there is a trade off between the measured data and the prior with increasing R_1. With $R_1 = 1.125$ in the second column in Figure 2.5, the heart and lung regions are almost perfect, and we still can see the copper pipe. With bigger truncation radius R_1, the copper pipe appears more clear. Note that the information of the copper pipe is included in the measured data only, but not in the prior. At the same time, with bigger R_1, there are more artifacts in general as expected. The use of a prior with bigger R_1 doesn't dramatically reduce the artifacts since the influence of the prior is reduced as R_1 increases. On the other hand, with moderate R_1 values, the effect of the inclusion of a prior is significant. Even though the conductivity values for each organ differ in the prior from the true values and don't include the pipes, the use of the prior sharpens the organ boundaries and reduces the artifacts, and even helps to see the presence of the pipe. Therefore, choosing the right value for R_1 is of importance. For SSIM values, we used Figure 2.1 (D) and (E) as the reference images. SSIM values for Figure 2.5 indicate that reconstructions with a prior are closer to the the reference image Figure 2.1 (D) than reconstructions without a prior. This is the same for the SSIM values of the first two columns of Figure 2.6. However, the SSIM values of the last two columns of Figure 2.6 demonstrate that the images with a prior are not closer to the reference image. This could be because the reference image Figure 2.1 (E) depicts the PVC pipe too sharply, while in the reconstructed images, the sharply contrasted conductivity inclusion, the PVC pipe in this case, appears very blurred.

2.5.3 Case (iii)

We also test our method on experimental tank data with three pieces of cucumber in the tank. The picture of the tank is shown in Figure 2.1 (C). Each slice of cucumber is about 4.9 cm in diameter. The data was collected using the ACE 1 system at 125 kHz with adjacent current patterns with amplitude 3.3 mA. The level of saline bath was 1.6 cm. Since cucumber has a cellular structure, and therefore a nonzero permittivity, $\gamma(x) = \sigma(x) + i\omega\epsilon(x)$ is now complex valued, and we reconstruct both the conductivity and the permittivity distributions at the same time. The conductivity of the saline bath was 0.180 S/m, but we had no information about the true conductivity and the permittivity of the cucumbers since our independent measurement device is for 1 kHz.

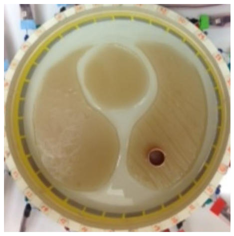

(A) Case (i)
: Copper pipe

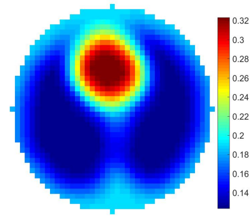

(B) Conductivity prior
with no pipe

R_1	Absolute image		Difference image	
	w/o a prior	with prior (B)	w/o prior	with prior (B)
1.125	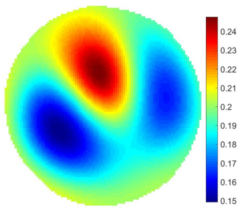 0.6267	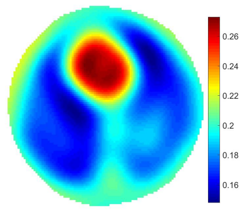 0.8131	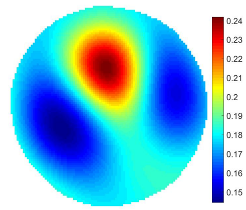 0.7926	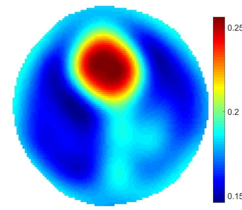 0.8760
1.35	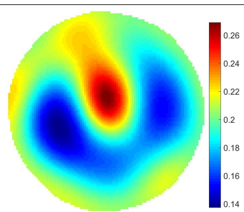 0.5993	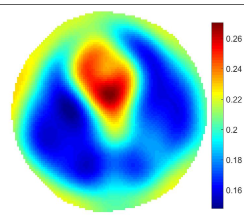 0.7097	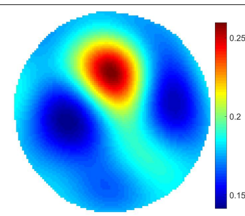 0.8343	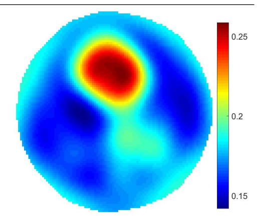 0.8491
1.575	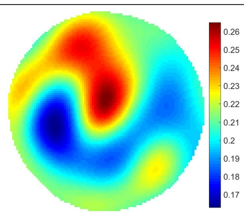 0.5629	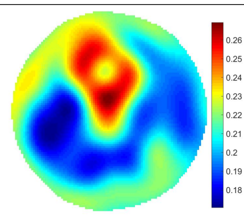 0.6606	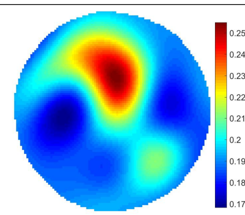 0.7860	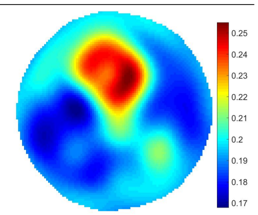 0.8009

Figure 2.5: The reconstructed images of Case (i). (A) is the picture of the case (i), (B) is the prior, which does not include the presence of the pipe. R_1 is $1.125, 1.35$ and 1.575 from the top row to the bottom row. $R_2 = 3$ for all cases. 1^{st} column is 2^{nd} order absolute images without a prior. 2^{nd} column is 2^{nd} order absolute images with a prior. 3^{rd} column is 2^{nd} order difference images without a prior. 4^{th} column is 2^{nd} order difference images with a prior. The values that are provided are the SSIM measures.

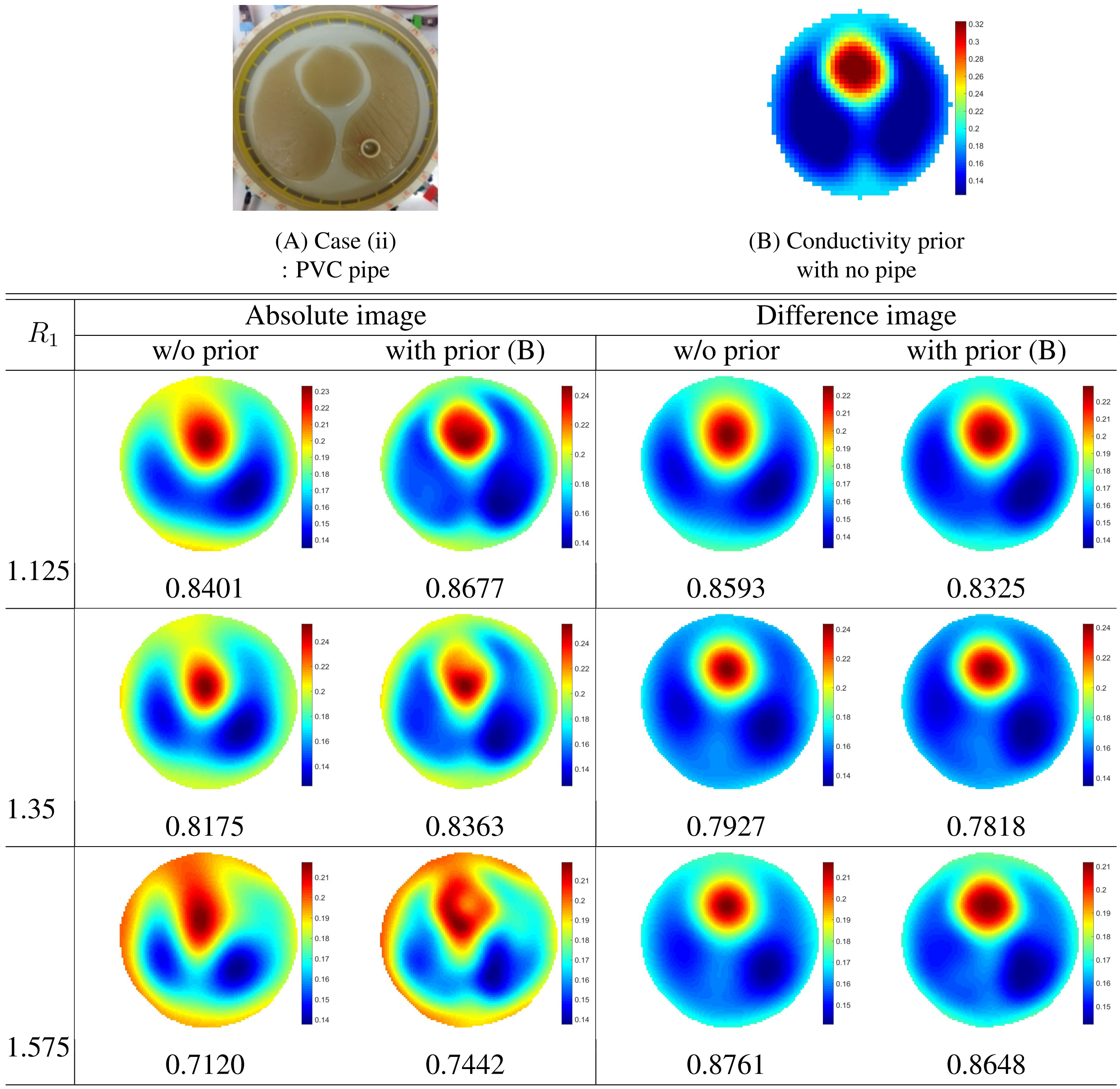

Figure 2.6: The reconstructed images of Case (ii). (A) is the picture of the tank, (B) is the prior, which does not include the presence of the pipe. R_1 is $1.125, 1.35$ and 1.575 from the top row to the bottom row. $R_2 = 3$ for all cases. 1st column is 2nd order absolute images without a prior. 2nd column is 2nd order absolute images with a prior. 3rd column is 2nd order difference images without a prior. 4th column is 2nd order difference images with a prior. The values that are provided are the SSIM measures.

2.5.4 Results and discussion for Case (iii)

Second order difference images of the cucumber data are shown in Figure 2.7. The real part of the prior is depicted in (B) and the imaginary part is in (C). The first two columns are for the real part of the reconstructions without and with a prior, respectively. The last two columns are the imaginary part of the reconstructions without and with a prior, respectively. We used the prior (B) and (C) as the reference images for the SSIM values. The effect of a prior inclusion can be interpreted as the same way as in the other cases.

2.6 Conclusions

We have presented a higher order Calderón's method based on its relationship to the D-bar method that is easy to compute. Its improvement over the original Calderón's method is demonstrated on experimental data. Furthermore, a method of including *a priori* spatial information is introduced and demonstrated on experimental tank data with complex conductivities. The methods and results provide new insight into Calderón's method and suggest that the higher order method with a prior could be a competitive alternative to existing direct and iterative methods for the computation of absolute images in electrical impedance tomography.

Acknowledgments

Research reported in this publication was supported by the National Institute Of Biomedical Imaging And Bioengineering of the National Institutes of Health under Award Numbers R21EB024683 and R01EB026710. The content is solely the responsibility of the authors and does not necessarily represent the official views of the National Institutes of Health.

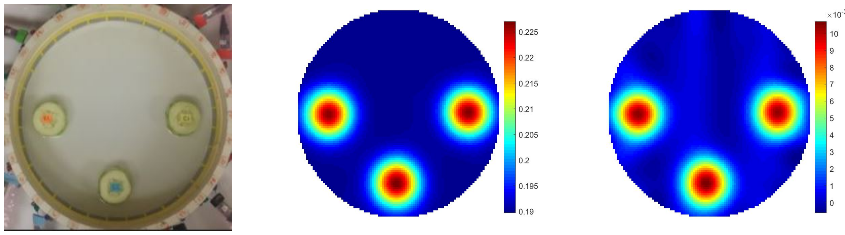

(A) Case (iii) (B) Real prior (C) Imaginary prior

R_1	Real part		Imaginary part	
	w/o prior	with prior	w/o prior	with prior
1.125	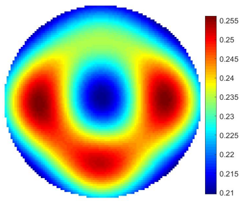 0.40035	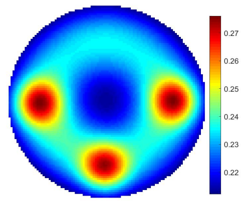 0.4383	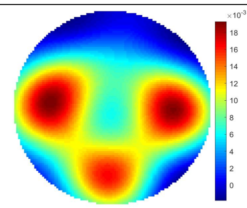 0.5781	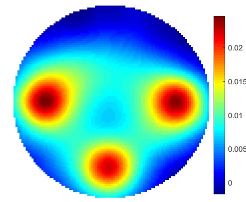 0.6950
1.35	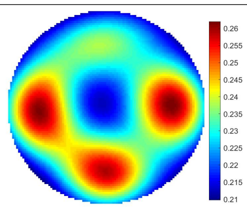 0.52792	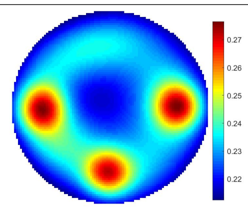 0.7504	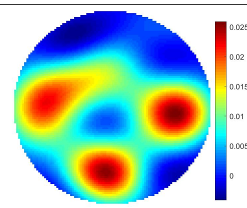 0.6257	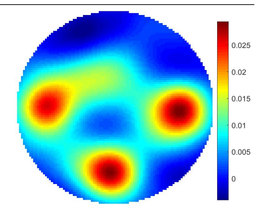 0.7130
1.575	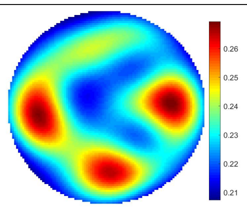 0.58512	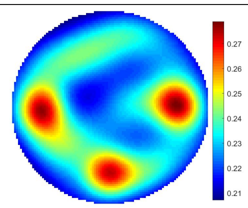 0.6865	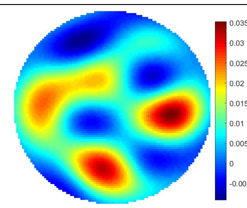 0.6739	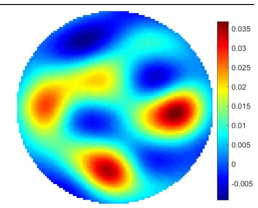 0.6975

Figure 2.7: The 2^{nd} order difference images of Case (iii) with and without a prior. (A) is the picture of Case (iii), (B) is the real part of the prior and (C) is the imaginary part of the prior. R_1 is $1.125, 1.35$ and 1.575 from the top row to the bottom row. $R_2 = 3$ for all cases. 1^{st} column is the real part of the images without a prior. 2^{nd} column is the real part of the images with a prior. 3^{rd} column is the imaginary part of the images without a prior. 4^{th} column is the imaginary part of the images with a prior. The values that are provided are the SSIM measures.

Chapter 3

Paper 2: Calderón's method with correct electrode location for the absolute image

Electrical impedance tomography (EIT) is a non-destructive imaging technique in which electrical measurements on the electrodes attached to the boundary of a subject are used to reconstruct the electrical properties of the subject. It has been demonstrated that various EIT reconstruction algorithms are very sensitive to the measurement and incorrect modeling of the boundary shape. Calderón's method is the seminal reconstruction algorithm that is direct, linearized, and fast, which uses a special type of harmonic functions. Calderón's method has been previously implemented with correct boundary shape, but the exact location of the electrodes have been disregarded as they are assumed to be spaced uniformly in angle. In this paper, we implement Calderón's method with a new expansion technique which enables the use of the correct location of the electrodes as well as the shape of the boundary resulting in improved absolute images.

2010 Mathematics Subject Classification : Primary 35J65, 35J25; Secondary 65N21.
Keywords: Electrical impedance tomography, Calderon's method, Inverse problems.

3.1 Introduction

Electrical impedance tomography (EIT) is an imaging modality that is not invasive and safe for living subjects. Mathematically, it is governed by the inverse conductivity problem which is a kind of the Cauchy problem in which the goal is to find some parameters (variable coefficients) in the given partial differential equation by using the knowledge of the boundary information. The typical situation in EIT is to apply some patterns of current through a finite number of electrodes attached to the boundary of a subject and measure the arising voltage distribution at the same time and reconstruct the electrical conductivity by using the measurement. Applications of EIT include medical imaging, such as detection of breast tumors and monitoring of pulmonary and lung functions, geophysical applications, and nondestructive testing. For a comprehensive list of applications, see [55] and references therein.

Despite the fact that EIT is a safe measurement technique for the patients, inexpensive, and portable, its practical application is still limited because the problem is very ill-posed in the sense that the reconstructed images are very sensitive to the measurement and modeling error. For example, it has been demonstrated that the use of the inaccurate boundary shape results in large systematic artifacts in the reconstruction. See [47, 56, 58, 62], for example. EIT is also a nonlinear inverse problem with respect to the measured data, and this makes the problem difficult to solve directly.

Calderón's method is a direct, linearized, and fast reconstruction algorithm. In [12], Calderón proved the unique solvability of a linearized inverse conductivity problem by using a special kind of harmonic functions, now known as *Complex Geometrical Optic (CGO)* solutions. His proof gives a linearized reconstruction algorithm and has led to the study of the inverse conductivity problem and its applications in many areas. We call the method in his paper *Calderón's method*. The first computational implementation of Calderon's method with simulated and experimental data collected with a circular tank was done in [8]. Calderón's method on a non-circular symmetric domain was implemented in [56], and the effect of the boundary modeling was studied. Implementations of Calderón's method on an asymmetric chest shaped domain, and for a human subject data was done in [57, 58] and the effect of the boundary modeling was studied. Yet, in [56–58], the location of the electrodes is assumed to be spaced uniformly in angle, which is incorrect.

The study of CGO solutions has generalized to the family of the D-bar reconstruction algorithms which solve the full nonlinear EIT problem directly. See [2–5, 39, 46, 48, 54, 60, 68] and [55] and references therein. It has been shown in [46] that Calderón's method is a three-step linearization of the D-bar method.

The computational complexity of Calderón's method and the D-bar method mainly comes from the expression of CGO solutions in terms of the measured data. In [58] and most of the other algorithms in the papers mentioned above, GGO solutions are expressed as a series of a set of trigonometric basis functions. Because many EIT systems are not able to apply the trigonometric current patterns directly, the technique of the change of basis is used to synthesize the voltage that would have been measured if we had applied the trigonometric current patterns.

In this paper, we implement an algorithm that takes into account the correct location of the electrodes to Calderón's method. To this end, we first extract the exact location of the electrodes from a photograph of the experimental tank, then compute CGOs at the location of electrodes and expand them with respect to the original current patterns and the measured voltage data directly, avoiding the synthesis of the data with respect to the trigonometric current patterns. We compare the results by using the exact location of electrodes with the results from the algorithm in [58] in which the location of the electrodes are ignored as they are assumed to be spaced uniformly in angle. We demonstrate that implementing the location of electrodes results in good absolute images. This paper is organized as follows. In Section 3.2, the mathematical formulation of EIT problem and Calderón's method is explained. The technique for numerical implementation is explained in Section 3.3. Experimental results are given in Section 3.4, and conclusions in Section 3.5.

3.2 Background

3.2.1 Modeling of EIT

Let $\gamma(x) \geq \gamma_0 > 0$ be the electrical conductivity with positive constant lower bound γ_0, $u(x)$ be the electrical potential, and $\Omega \in \mathbb{R}^2$ be a bounded domain. Since $\nabla \cdot \gamma(x)\nabla u(x)$ is the source of the current at each point x, and the body is current source free, the governing equation of EIT is

$$\nabla \cdot \gamma(x)\nabla u(x) = 0, \; x \in \Omega. \tag{3.1}$$

This equation can be derived analytically by using the Maxwell's equations [55]. The applied current density j on the boundary is then

$$\gamma(x)\frac{\partial u}{\partial \nu}(x) = j(x), \;\; x \in \partial\Omega, \tag{3.2}$$

where ν is the outward normal vector to $\partial\Omega$, and this is the Neumann boundary condition for (3.1). We denote the voltage distribution on the boundary by f so that

$$u(x) = f(x), \quad x \in \partial\Omega, \tag{3.3}$$

which is the Dirichlet boundary condition for (3.1). If $\gamma(x)$ and one of the boundary conditions (3.2) or (3.3) are given, the forward problem is to solve for $u(x)$ in Ω. The inverse problem is to find the unknown $\gamma(x)$ provided that the two boundary conditions (3.2) and (3.3) are given. In practical applications, in order to make the reconstruction algorithm robust, we apply a set of current patterns through a finite number of electrodes and measure the arising voltage distributions on all of the electrodes at the same time. Therefore, the data to be used is the Neumann-to-Dirichlet (ND) map,

$$\mathcal{R}_\gamma : \gamma(x)\frac{\partial u}{\partial \nu}(x) \longrightarrow u(x), \; x \in \partial\Omega,$$

which is also called the current density-to-voltage map. However, in most of the mathematical literature, the theory is developed by using the Dirichlet-to-Neumann (DN) map

$$\Lambda_\gamma : u(x) \longrightarrow \gamma(x)\frac{\partial u}{\partial \nu}(x), \; x \in \partial\Omega, \tag{3.4}$$

which is also called the voltage-to-current density map.

3.2.2 Calderón's method

We summarize Calderón's method in [12]. Calderón assumed that $\gamma(x)$ is a small perturbation from the background conductivity 1 so that $\gamma(x) = 1 + \delta(x)$, where $\delta(x)$ is a small perturbation in

$L^\infty(\Omega)$. Calderón's method uses the special type of harmonic functions

$$f(x;k,a) = e^{\pi i(k\cdot x)+\pi(a\cdot x)}, \quad g(x;k,a) = e^{\pi i(k\cdot x)-\pi(a\cdot x)},$$

where $k, a \in \mathbb{R}^2$ are nonphysical frequency variables with $|k|= |a|, \;\; k\cdot a = 0$. These constraints for k, a are to make the two functions be harmonic, meaning that $\Delta f = \Delta g = 0$. These type of functions are now known as *Complex Geometrical Optic* (CGO) solutions. The main idea of Calderón's method is that when we apply the voltages f and g on the boundary $\partial\Omega$, the arising potential distributions $\omega_i(i = 1, 2)$ of the body are small perturbations from f and g provided that $||\delta||_{L^\infty(\Omega)}$ is small. We denote ω_i on Ω as

$$\omega_i = u_i + v_i \text{ in } \;\Omega,$$

where $\omega_1 = f$ and $\omega_2 = g$ on $\partial\Omega$, $u_i \in H^1(\Omega)$, and $v_i \in H^1_0(\Omega)$ for $i = 1, 2$. Here H^1 denotes the Sovolev space and H^1_0 the Sovolev space with trace zero. Then, by (3.1) and integration by parts,

$$\begin{aligned}
\int_{\partial\Omega} f(x,k)\Lambda_\gamma g(x,k)\mathrm{d}s(x) &= \int_{\partial\Omega} w_1\gamma\frac{\partial\omega_2}{\partial\nu}\mathrm{d}s(x) \\
&= \int_{\Omega} \gamma(\nabla\omega_1\cdot\nabla\omega_2)\mathrm{d}x \\
&= \int_{\Omega} \gamma\nabla u_1\cdot\nabla u_2 + \delta(\nabla u_1\cdot\nabla v_2 + \nabla u_2\cdot\nabla v_1) + \gamma\nabla v_1\cdot\nabla v_2\mathrm{d}x \\
&= -2\pi^2|k|^2\int_{\Omega}\gamma(x)\exp\left[2\pi i x\cdot k\right]\mathrm{d}x + \tilde{R}(k).
\end{aligned}$$

Therefore, from the first line and the last line of the above equations, we get

$$\int_\Omega \gamma(x)\exp\left[2\pi i x\cdot k\right]\mathrm{d}x = -\frac{1}{2\pi^2|k|^2}\int_{\partial\Omega} f(x,k)\Lambda_\gamma g(x,k)\mathrm{d}s(x) + \frac{\tilde{R}(k)}{2\pi^2|k|^2}.$$

When we assume $\gamma(x)$ is constant outside of Ω. The left-hand side is the Fourier transform of $\gamma\chi_\Omega$, which we denote by $\hat{\gamma}(k)$. We denote the first term on the right-hand side by

$$\hat{F}_\gamma^{\text{abs}}(k) = -\frac{1}{2\pi^2|k|^2}\int_{\partial\Omega} f(x,k)\Lambda_\gamma g(x,k)\mathrm{d}s(x), \tag{3.5}$$

and the last term by $\hat{R}(k)$. Calderón showed that when $||\delta(x)||_{L^\infty(\Omega)}$ is small, $|\hat{R}(k)|$ is small for small values of $|k|$. Since $\gamma(x)\chi_\Omega$ is zero outside of Ω, $|\hat{\gamma}(k)|$ has to decrease to zero as $|k|$ gets large. Therefore, by multiplying a mollifying function $\hat{\eta}(k)$ such that $\hat{\eta}(0) = 1$, $\hat{\eta} \in C^\infty$ and that decreases fast to zero as $|k|$ gets large, $\hat{F}_\gamma^{\text{abs}}\hat{\eta}$ approximates $\hat{\gamma}$, and it is shown in [12] that the inverse Fourier transform of $\hat{R}(k)\hat{\eta}(k)$ is negligible when $||\delta||_{L^\infty}$ is small. The use of the mollification accounts to passing $\hat{F}_\gamma^{\text{abs}}$ to a low-pass filter. This low-pass filtering can be done alternatively by truncating $\hat{F}_\gamma^{\text{abs}}(k)$ into a disk of radius R_T. We call R_T the truncation radius. Therefore, we get an approximation of $\gamma(x)$ by

$$\gamma(x) \approx \int_{|k|\le R_T} \hat{F}_\gamma^{\text{abs}}(k)e^{-2\pi i x\cdot k}dk. \tag{3.6}$$

We call the reconstruction from (3.6) *the absolute image of* γ. By the similar calculation, we define

$$\hat{F}_\delta^{\text{diff}}(k) = -\frac{1}{2\pi^2|k|^2}\int_{\partial\Omega} f(x,k)(\Lambda_\gamma - \Lambda_1)g(x,k)\mathrm{d}s(x), \tag{3.7}$$

and we get an approximation of $\delta(x)$ by

$$\delta^{\text{diff}}(x) \approx \int_{|k|\le R_T} \hat{F}_\delta^{\text{diff}}(k)e^{-2\pi i x\cdot k}dk, \tag{3.8}$$

and call it *the difference image of* δ. But the computation of the difference image requires knowledge of Λ_1, which we call the *the homogeneous data*. In practical applications such as medical imaging, Λ_1 cannot be measured. On the other hand, since

$$\int_\Omega f\Lambda_1 g \mathrm{d}x = -2\pi^2|k|^2\int_\Omega e^{2\pi ik\cdot x}\mathrm{d}x,$$

(3.7) can be replaced by

$$\hat{F}^{\text{abs}}_\delta(k) = -\frac{1}{2\pi^2|k|^2}\int_{\partial\Omega} f(x,k)\Lambda_\gamma g(x,k)\mathrm{d}s(x) - \int_\Omega e^{2\pi ik\cdot x}\mathrm{d}x. \tag{3.9}$$

We define

$$\delta^{\text{abs}}(x) \approx \int_{|k|\leq R_T} \hat{F}^{\text{abs}}_\delta(k)e^{-2\pi ix\cdot k}dk, \tag{3.10}$$

and call it the *the absolute image of* δ. While one can compute $\gamma(x)$ directly by using (3.6), the reason why we use (3.8) or (3.10) is to avoid the Gibbs phenomena near $\partial\Omega$. Notice that $\gamma(x)\chi_\Omega$ is sharply discontinuous along $\partial\Omega$, and that introduces the Gibbs phenomena along $\partial\Omega$ in the reconstructed images. On the other hand, since $\delta(x)$ can be assumed to be zero and therefore flat near $\partial\Omega$, there are no Gibbs phenomena in the reconstructed images. This Gibbs phenomena in the absolute images of γ can be observed in [8] and also is demonstrated later in this paper. For the computation of the inverse Fourier transform, we use the Simpson's quadrature rule.

3.3 Numerical implementation

In this paper, we use data collected on a chest shaped tank described below. See Figure 3.1. There are 32 electrodes on the boundary of the tank. We denote the number of electrodes by L in the following lines. For $i = 1,\ldots,L-1,\ \ l = 1,\ldots,L$, let T^i_l denote the i^{th} current pattern on l^{th} electrode and V^i_l the measured voltage. We require that T^i and V^i satisgy $\sum_{l=1}^L T^i_l = \sum_{l=1}^L V^i_l = 0$. Let t^i denote the normalized current $t^i = (T^i)/(||T^i||_2)$ and v^i the normalized voltage $v^i = (V^i)/(||T^i||_2)$, where $||T^i||_2 = \sqrt{\sum_{l=1}^L (T^i_l)^2}$. In this paper, the adjacent current patterns were applied on the electrodes and are given by

$$T_l^i = \begin{cases} M, & l = i, \\ -M, & l = i+1, \end{cases}$$

where M is the amplitude of the current patterns. We model the current density $j(x)$ on the boundary by the gab model given by

$$j(x) = \begin{cases} \frac{I_l}{A}, & x \in e_l, \\ 0, & \text{otherwise}, \end{cases}$$

where e_l denotes the l^{th} electrode and A is the area of an electrode, which is assumed to be the same for all electrodes. Let $x|_{\partial\Omega} = (x_1(\theta), x_2(\theta)) = r(\theta)(\cos\theta, \sin\theta)$ be a parameterization of the boundary by θ, and the line element $s(\theta)d\theta = \sqrt{(x_1')^2 + (x_2')^2}d\theta = \sqrt{r^2 + (r')^2}d\theta$. Denote the angle of electrodes by $(\theta_l)_{l=1}^{l=L}$ and gab between them by $\Delta\theta_l = \theta_{l+1} - \theta_l$. For functions r, s of θ such that $r, s : \mathbb{R}^L \to \mathbb{R}$, let $(r(\cdot), s(\cdot))_L$ denote the discrete inner product defined by $(r(\cdot), s(\cdot))_L = \sum_{l=1}^{L} r(\theta_l)s(\theta_l)$. We first obtain the location of the electrodes by using a photograph of the tank, Figure 3.1, and compute $f(x_l, k)$ and $g(x_l, k)$ at those points for each k. Then, we expand $f(x_;, k)$ and $g(x_l, k)$ with respect to the normalized current patterns and the measured voltages as

$$f(x_l, k) = \sum_{i=1}^{L-1} f_k^i t_l^i, \tag{3.11}$$

$$g(x_l, k) = \sum_{j=1}^{L-1} g_{k,\gamma}^j v_l^{j,\gamma}, \tag{3.12}$$

and let $\mathbf{f}_k = \{f_k^i\}_{i=1}^{L-1}$ and $\mathbf{g}_{k,\gamma} = \left\{g_{k,\gamma}^j\right\}_{j=1}^{L-1}$ denote the coefficient vectors, where the subscripts k and γ indicate the dependence of the coefficients on the variable k and the conductivity γ. Since the applied normalized current patterns and the measured voltages are not orthogonal in general, in order to compute $\mathbf{f}_k$ and $\mathbf{g}_{k,\gamma}$, we need to solve systems of linear equations. By taking the inner product with $v^{i,\gamma}$ $(i = 1, 2, ..., L-1)$ on both sides of (3.12), we get $\mathbf{V}_\gamma \mathbf{g}_{k,\gamma} = \mathbf{c}_{k,\gamma}$, where $\mathbf{V}_\gamma(i,j) = (v^{i,\gamma}, v^{j,\gamma})_L$ and $\mathbf{c}_{k,\gamma}(i) = \left(g(x_l,k), v_l^{i,\gamma}\right)_L$. Therefore, $\mathbf{g}_{k,\gamma} = \mathbf{V}_\gamma^{-1}\mathbf{c}_{k,\gamma}$. Similarly, $\mathbf{f}_k = \mathbf{T}^{-1}\mathbf{d}_k$, where $\mathbf{T}(i,j) = (t^i, t^j)_L$ and $\mathbf{d}_k(i) = (f(x_l,k), t_l^i)_L$. Now, with (3.11) and (3.12),

$$\begin{aligned}
\int_{\partial\Omega} f(x,k)\Lambda_\gamma g(x,k)\mathrm{d}s(x) &= \int_0^{2\pi} \sum_{i=1}^{L-1} f_k^i t^i(\theta) \left[\Lambda_\gamma \sum_{j=1}^{L-1} g_{k,\gamma}^j v^{j,\gamma}(\cdot)\right](\theta)s(\theta)d\theta \\
&= \sum_{i=1}^{L-1}\sum_{j=1}^{L-1} f_k^i g_{k,\gamma}^j \int_0^{2\pi} t^i(\theta)\left[\Lambda_\gamma v^{j,\gamma}(\cdot)\right](\theta)s(\theta)d\theta \\
&= \frac{1}{A}\sum_{i=1}^{L-1}\sum_{j=1}^{L-1} f_k^i g_{k,\gamma}^j \sum_{l=1}^{L} t_l^i t_l^j e_w, \\
&= \frac{e_w}{A}\mathbf{f}_k^T \mathbf{T}\mathbf{g}_{k,\gamma},
\end{aligned}$$

where e_w is the width of one electrode, where all are assumed to be equal, and $\mathbf{f}_k^T$ is the transpose of $\mathbf{f}_k$. Notice that the coefficients $\mathbf{f}_k$ and $\mathbf{g}_{k,\gamma}$ encode the information about the location of electrodes and therefore the boundary shape provided that we use the exact values of $f(x_l,k)$ and $g(x_l,k)$ in (3.11) and (3.12). From (3.7), (3.9) and by the similar calculation,

$$\hat{F}_\delta^{\text{diff}}(k) = -\frac{e_w}{2\pi^2 A|k|^2}\mathbf{f}_k^T \mathbf{T}(\mathbf{g}_{k,\gamma} - \mathbf{g}_{k,1}), \tag{3.13}$$

and

$$\hat{F}_\delta^{\text{abs}}(k) = -\frac{e_w}{2\pi^2 A|k|^2}\mathbf{f}_k^T \mathbf{T}\mathbf{g}_{k,\gamma} - \int_\Omega e^{2\pi i k\cdot x}\mathrm{d}x. \tag{3.14}$$

3.4 Experimental results

We test the proposed algorithm with the data that is used in [58] in order to demonstrate the improvement of the absolute images by comparing the results from the proposed algorithm with the results from the algorithm in [58]. Figure 3.1 is the photo of the tank of which the perimeter is 1.016 m, simulating the shape of a human subject. The tank is filled with saline of conductivity of 0.2 S/m to a height of 0.0204 m, and three inclusions featuring two lungs of conductivity 0.09

S/m and the heart of conductivity 0.45 S/m. The width of the electrodes is 0.254 m. From the center of the tank, the electrodes are spaced non-uniformly in angle. For the homogeneous data for the difference images of δ, a data set is collected with only saline in the tank. The data was taken with the Active Complex Electrode (ACE1) system (see, [51, 52]) in the EIT lab at Colorado State University. The frequency of the system was 125 kHz and the current amplitude was 3.3 mA.

Figure 3.1: The chest shaped tank filled with saline bath and inclusions simulating two low conductive lungs and the high conductive heart.

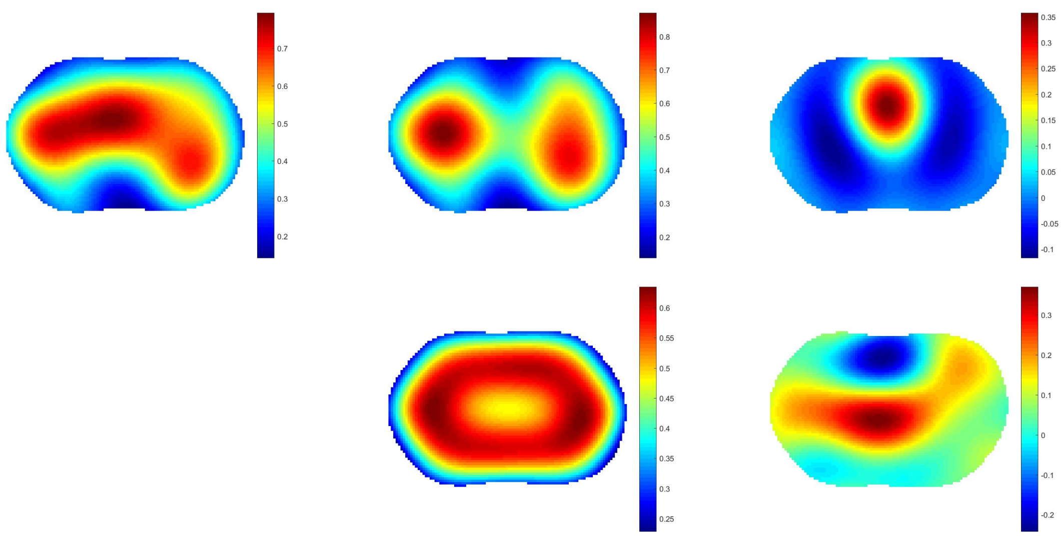

Figure 3.2: Reconstructions without modeling the location of electrodes. Top left: An absolute image of γ. Top middle: An absolute image of the homogeneous tank from the homogeneous tank data. Top right: A difference image of δ. Bottom middle: A synthesized image of homogeneous tank. Bottom right: An absolute image of δ.

Figure 3.2 depicts reconstructions with the algorithm suggested in [58] in which the location of electrodes is assumed to be spaced uniformly in angle. The top left image is an absolute image of γ. The top middle image is a reconstruction of the saline-filled homogeneous tank using the measured homogeneous data. The top right image is the difference of the previous two images, the difference image of δ. The bottom middle image is a synthesized background conductivity by using a quadrature rule for the second term in (3.14) and taking the inverse Fourier transform of that. The bottom right image is the difference of top left and bottom middle images, an absolute image of δ.

The first thing to notice is that, since the conductivity distribution is discontinuous along the boundary, the three leftmost images show the Gibbs phenomena along the boundary as there appear blue rings along the boundary, and these low conductive artifacts severely deteriorate the reconstructions. Second, there are artifacts due to incorrect electrodes modeling. In the top middle figure, there are two big red blobs on both sides of the image. Since it is the reconstruction from the homogeneous tank data, it should look like the bottom middle figure. But, the one red region across the tank in the bottom middle figure is separated into two big blobs in the top middle figure. These are the artifacts as a result of the incorrect modeling of the electrode location. That artifact seems to appear in the top left, making the region of low conductive lungs appear as high conductive. Consequently, these artifacts in the first two images in the top row get subtracted in the top right image, the difference image of δ. In that difference image, we see two lungs and the heart quite clearly. On the other hand, the same kind of artifact doesn't appear in the synthesized background conductivity distribution in the bottom middle image, consequently, the artifact in the top left is not subtracted effectively in the bottom right image, resulting in a poor absolute image of δ. The truncation radius is 1.4 for all images. The same situation happens with different truncation radius and we are not able to get a reasonable absolute image without using the correct location of electrodes.

Figure 3.3 depicts the difference images of δ and the absolute images of δ with correct electrode modeling suggested in this paper, i.e., the exact location of the electrodes is used in the reconstruc-

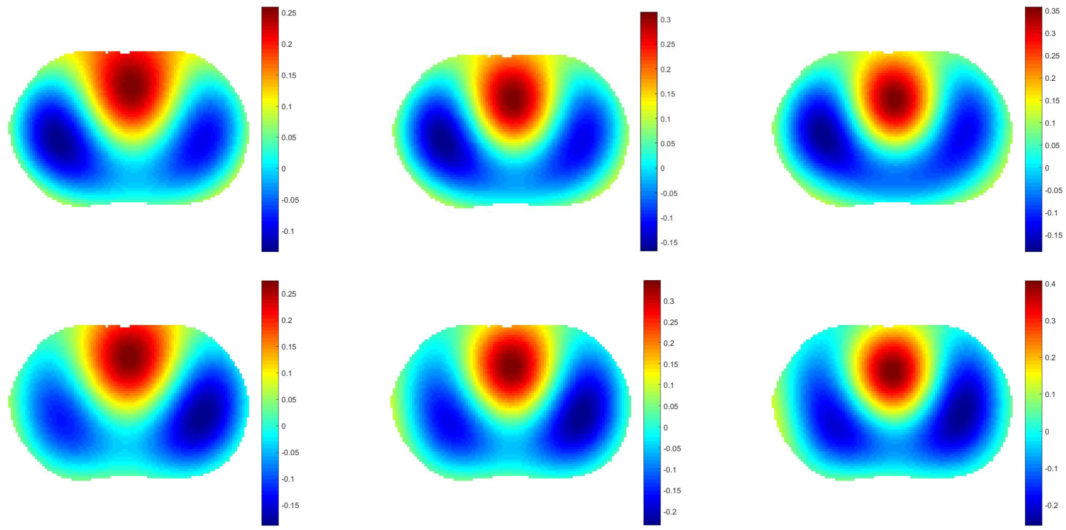

Figure 3.3: Reconstructions with modeling the location of electrodes. Top row: Differences images of δ. Bottom row: Absolute images of δ. The truncation radius are 1, 1.1 and 1.2 for each column from the left to the right.

tion. The top row shows the difference images of δ with the truncation radius 1, 1.1, and 1.2 from the left to the right. The bottom row shows the absolute images of δ with the same truncation radius as the top row, respectively. With correct electrodes modeling, we get good absolute images of δ as we can see in the bottom row: the two lungs and the heart appear clearly in the images, and this is no worse than the difference images at the top row.

3.5 Conclusions

With incorrect modeling of the electrodes, there are inevitable artifacts in the absolute image of γ, and these artifacts cannot be removed by subtracting the synthesized background conductivity which makes it impossible to get a reasonable absolute image. On the other hand, the same kind of artifact doesn't appear with the correct electrode modeling, and we can get good absolute images by subtracting the synthesized background conductivity. In this case, the absolute images of δ are no worse than the difference images of δ.

Chapter 4

Paper 3: Three dimensional Calderón's method for EIT on the cylindrical geometry

Electrical impedance tomography (EIT) is an imaging modality in which voltage data arising from currents applied on the boundary are used to reconstruct the conductivity distribution in the interior. Calderón's seminal paper on the inverse conductivity problem provided equations for a direct linearized inversion method. This paper provides the first implementation of Calderón's method on a 3-D cylindrical domain with data collected on a portion of the boundary. The effectiveness of the method to localize inhomogeneities in the plane of the electrodes and in the z-direction is demonstrated on simulated and experimental data.

2010 Mathematics Subject Classification : Primary 35J65, 35J25; Secondary 65N21.
Keywords: Partial differential equations, Calderon's method, electrical impedance tomography, finite element method, inverse problems.

4.1 Introduction

Electrical impedance tomography (EIT) is a non-invasive, non-ionizing imaging technique in which the conductivity distribution in the interior of the body is reconstructed from measurements of surface voltages resulting from the application of an AC current. The most widely developed application of EIT is for pulmonary imaging for which several commercial systems existing worldwide are used for monitoring patients receiving mechanical ventilation in the ICU. The reader is referred to the articles [28, 49, 61] for comprehensive reviews on EIT for lung imaging.

The typical electrode configuration for pulmonary imaging with EIT is a belt or ring of electrodes placed around the circumference of the patient's chest, and the conductivity is reconstructed in the plane of the electrodes as a single cross-sectional image. This approach has several well-known shortcomings, however. First, the flow of current is not confined to the plane of the electrodes and as a result, objects that are out-of-plane are projected into the in-plane image [9,23,35,65]. Indeed, by adding a single electrode ring and using 3-D current patterns, the artefact from an out-of-plane target can be reduced from 35% to 10% of the target value [9]. Studies comparing two row to single row electrode configurations on tidal ventilation in a horse support this finding [34]. Second, a 2-D slice has no resolution in the caudocranial direction, and so pathologies may be masked or superimposed in the image, and their exact location and volume cannot be determined.

There are several iterative approaches to 3-D reconstruction on a torso, usually modeled as a cylinder as is done here. The ToDLeR algorithm [9] takes a linearized one-step approach inspired by the 2-D NOSER algorithm [16], and [79] uses a one-step Gauss-Newton iteration with generalized Tikhonov regularization. Gauss-Newton reconstructions on a chest-shaped domain can be found in [13, 49]. In this work, we introduce an implementation of Calderón's method, which is a direct (non-iterative) linearized method, to compute the conductivity in a cylindrical domain on two to four rings of electrodes. Calderón's seminal paper [12] has inspired a wealth of mathematical research on the inverse conductivity problem. Not only has the tool of special exponentially growing solutions known as *complex geometrical optics* (CGO) solutions helped find answers to questions of global uniqueness and stability, it has inspired the creation of a new family of direct methods for EIT known as D-bar methods. The reader is referred to [55] for more information about D-bar methods.

The two dimensional (2-D) Calderón's method was first implemented on a circle for experimental data in [8]. The artefacts caused by approximating an elliptical domain by a circle were quantified in [56]. The 2-D method was implemented for human data on a subject-specific domain in [58]. Reconstruction of the complex valued admittivity can be found in [14,15,57]. The only implementation of Calderón's method in three dimensions is in the mammography geometry [10,20].

This is the first paper to provide a version of Calderón's method for data measured on a portion of the boundary of a cylinder. For this novel implementation, we focus on the case of a real-valued conductivity, although the method is extendable to $\gamma(x) \in \mathbb{C}$. The method is tested on simulated data with two and four rows of electrodes and is demonstrated to be robust in the presence of noise, which is further seen from reconstructions of data collected on a saline-filled tank. The purpose of this paper is to present the algorithm and demonstrate that it is effective for identifying reconstructions in the plane of the electrodes with resolution in the z-direction that improves as the number of rows of electrodes increases. A study of the robustness to modeling errors and a comparison to other algorithms is a topic of future work.

4.2 Background

4.2.1 Governing equations

Let $\gamma(x)$ be the electrical conductivity, $u(x)$ be the electrical potential and $\Omega \subset \mathbb{R}^3$ be a bounded domain with Lipschitz boundary $\partial\Omega$. Then since $\gamma(x)\nabla u(x)$ is the current and we assume the body itself is current source free, the governing equation of the electrical impedance tomography problem is

$$\nabla \cdot \gamma(x)\nabla u(x) = 0, \; x \in \Omega. \tag{4.1}$$

We denote the class of admissible conductivities as

$$Q = \{\gamma \in L^\infty(\Omega) | \gamma(x) \geq \gamma_0 > 0, \text{ for } x \in \Omega \text{ and } \gamma_0 \in \mathbb{R}\}.$$

The applied current density j on the boundary is then

$$\gamma(x)\frac{\partial u}{\partial \nu}(x) = j(x), \;\; x \in \partial\Omega, \tag{4.2}$$

where ν is the outward normal vector to $\partial\Omega$, and this corresponds to the Neumann boundary condition. Equations (4.1) and (4.2) are known as the *continuum model* for EIT. The induced voltage f by the application of the current density j on the boundary $\partial\Omega$ is

$$u(x) = f(x), \quad x \in \partial\Omega, \tag{4.3}$$

and this corresponds to the Dirichlet boundary condition. In practical implementation, it is the current density-to-voltage map, also called the Neumann-to-Dirichlet map, that is used to find $\gamma(x)$. However, in most of the mathematical literatures for the inverse conductivity problem, it is the Dirichlet-to-Neumann map, or voltage-to-current density map

$$\Lambda_\gamma : u|_{\partial\Omega} \to \gamma(x)\frac{\partial u}{\partial \nu}\bigg|_{|\partial\Omega},$$

that is used for the theoretical development. The inverse conductivity problem is to find the unknown $\gamma(x)$ provided that Λ_γ is known.

4.2.2 Complete Electrode Model

In practice, the continuum model is not a good model for experimental data [18], and the complete electrode model (CEM) was developed to account for discrete electrodes and the electrochemical effect between the electrodes and the body. We use the CEM for the simulated data in this work and briefly summarize it here.

Suppose L electrodes have been fixed around the surface of an object. In an EIT experiment, a basis of current patterns is applied on the electrodes, and the resulting voltage is measured on all of the electrodes. Equation (4.1) is used to solve for the electric potential on the electrodes and inside Ω given an applied current I.

In practice, the current density j at the electrodes is unknown, but $\int_{E_l} \gamma \frac{\partial u}{\partial \nu} dS = I_l$ is known, where ν is the unit outward normal to Ω, E_l is the surface area of the lth electrode and I_l is the current injected into E_l. Then the Neumann condition (4.2) can be rewritten as

$$\int_{E_l} \gamma \frac{\partial u}{\partial \nu} dS \quad = \quad I_l \quad \text{for } l = 1, 2, ..., L, \tag{4.4}$$

$$\gamma \frac{\partial u}{\partial \nu} \quad = \quad 0 \quad \text{on } \partial\Omega / \cup_{l=1}^{L} \overline{E_l}, \tag{4.5}$$

since the current density is 0 on the boundary off the electrodes. Since the electrodes themselves provide a low-resistance path for the current to pass, the potential on each electrode is modeled as constant: $U_l =$ constant. This property is known as the *shunting effect*, which is represented by

$$u = U_l, \text{ on } E_l, \text{ for } l = 1, 2, ..., L. \tag{4.6}$$

The electrochemical effect referred to above is due to the formation of a thin and highly resistive layer between the electrodes and the body. Electrical impedance from this layer, z_l, is called the effective contact impedance or surface impedance at E_l. This effect changes (4.6) to

$$u + z_l \gamma \frac{\partial u}{\partial \nu} = U_l \quad \text{on } E_l \text{ for } l = 1, 2, ..., L. \tag{4.7}$$

The CEM consists of (4.1), (4.4), (4.5) and (4.7), together with the following conditions.

$$\sum_{l=1}^{L} I_l \quad = \quad 0 \quad \text{(conservation of charge)}$$

$$\sum_{l=1}^{L} U_l \quad = \quad 0 \quad \text{(choice of a ground)}$$

In [17], it is shown that the accuracy of the CEM can closely match the measurement precision of experimental measurements. Existence and uniqueness of a solution to the CEM can be shown using the Lax-Milgram theorem [17], which shows that (u, U) satisfies (4.1), (4.4), (4.5) and (4.7) if and only if,

$$b((u,U),(v,V)) = g(v,V), \text{ for all } (v,V) \in H^1(\Omega) \oplus \tilde{\mathbb{R}}^L,$$

where $\tilde{\mathbb{R}}^L = \{x \in \mathbb{R}^L : \sum_i x_i = 0\}$, $b((u,U),(v,V))$ is a bilinear form defined as,

$$b((u,U),(v,V)) = \int_\Omega \gamma \nabla u \cdot \nabla v \mathrm{d}x + \sum_{l=1}^{L} \frac{1}{z_l} \int_{E_l} (u - U_i)(v - V_i) \mathrm{d}s,$$

and $g(v,V) = \sum_{l=1}^{L} I_l V_l$.

In order to solve the inverse problem, we need to solve the forward problem, i.e., given the parameter γ, find (u,U). We use the finite element method (FEM) for solving the forward model.

4.2.3 FEM discretization of CEM

Let $T = \{T_1, ..., T_{|T|}\}$ be the triangularization of Ω, which has n mesh points for the finite dimensional subspace H_n of $H_1(\Omega)$. Any $\tilde{u} \in H_n$ is represented by

$$u(x) \approx \tilde{u}(x) = \sum_{i=1}^{n} \alpha_i \phi_i(x), \text{ for } \alpha_i \in \mathbb{R},$$

where $\phi_i(x)$ are the basis functions of H_n satisfying $\phi_i(x_k) = \delta_{ik}$ for $i,k = 1,\dots,n$ and $x_k \in H_n(\Omega)$. The electric potential on the electrodes is given by

$$U \approx U^h = \sum_{k=1}^{L-1} \beta_k \zeta = G\beta,$$

where $\beta_k \in \mathbb{R},\ \zeta_k, k = 1,\dots,L-1$, comprise the basis for $\tilde{\mathbb{R}}^L$ and $G \in \mathbb{R}^{L\times(L-1)}$. We want to determine the coefficients α_i and β_k in this formulation. Choosing $v = \phi_i$ and $V = \zeta_k$ when the set of test functions is of the form $(\phi_1, 0), ..., (\phi_n, 0), (0, \zeta_1), ..., (0, \zeta_{L-1})$ results in the following system of equations in matrix form:

$$A\theta = q,$$

where $\theta = (\alpha, \beta)^T \in \mathbb{R}^{n+L-1}$, the matrix A is the standard FEM system matrix (see [80] for details), and the right hand side q is given by

$$q_i = \begin{cases} 0 & \text{for } i = 1, \ldots, n \\ I^T \zeta_{i-n} & \text{for } i = n+1, \ldots, n+L-1. \end{cases}$$

4.2.4 Current patterns

For the input current pattern, we use the current patterns derived in [9, 33] as the analytical solution to the forward problem (1), (2) with the continuum model. These patterns ensure that current flows between the rows of electrodes in 3-D. We follow the notations in [9]. Let J be the number of layers of electrodes and K be the number of electrodes in each layer. Then the total number of electrodes is given by $L = JK$. For $i = 1, \ldots, L$, let

$$I^i_{l,l_z} = \begin{cases} M_i \cos(k\theta_l), & \text{for } k = 1, \ldots, \frac{K}{2}; \\ M_i \cos(k\theta_l) \cos\left(\frac{j\pi}{b}\left(z_{l_z} - z_0 + \frac{b}{2}\right)\right), & \text{for } k = 1, \ldots, \frac{K}{2}; j = 1, \ldots, J-1; \\ M_i \cos\left(\frac{j\pi}{b}\left(z_{l_z} - z_0 + \frac{b}{2}\right)\right), & \text{for } j = 1, \ldots, J-1; \\ M_i \sin(k\theta_l), & \text{for } k = 1, \ldots, \frac{K}{2} - 1; \\ M_i \sin(k\theta_l) \cos\left(\frac{j\pi}{b}\left(z_{l_z} - z_0 + \frac{b}{2}\right)\right), & \text{for } k = 1, \ldots, \frac{K}{2}; j = 1, \ldots, J-1; \end{cases}$$

here, $\theta_l = \frac{2\pi l}{K}$, z_{l_z} is the distance from the bottom of the tank to the center of the l_z^{th} layer, I^i_{l,l_z} is the i^{th} current pattern applied to the l^{th} electrode of the l_z^{th} layer, b is the height of the vertical span of the electrodes; distance from the bottom of the lowest layer to the top of the uppermost layer, and M_i is the normalizing constant with which $\|I^i_{l,l_z}\|_{L^2} = 1$. We denote the corresponding voltage distribution on the boundary due to the conductivity distribution γ by $U^{i,\gamma}_{l,l_z}$.

4.2.5 Calderón's method

Calderón's method is based on the linearization of the inverse problem with the assumption that $\gamma(x) = 1 + \delta(x)$, where $\delta(x)$ is a small perturbation from the background conductivity 1. Calderón used the special family of harmonic functions

$$\psi_1(x,k,a) = e^{i\pi(x\cdot k)+\pi(a\cdot x)}, \tag{4.8}$$

$$\psi_2(x,k,a) = e^{i\pi(x\cdot k)-\pi(a\cdot x)}, \tag{4.9}$$

where $k, a \in \mathbb{R}^3$ are nonphysical frequency variables that are related as $|k| = |a|, \quad k \cdot a = 0$. These conditions guarantee that $\Delta\psi_1 = \Delta\psi_2 = 0$. We consider the cases of applying potential distributions (4.8) and (4.9) on the boundary $\partial\Omega$, and denote the resulting potential distributions on Ω as

$$\omega_i = u_i + v_i \text{ in } \Omega,$$

where $u_i = \psi_i$ on Ω, and $v_i \in H_0^1(\Omega)$ for $i = 1, 2$. Here H^1 denotes the Sobolev space and H_0^1 the Sobolev space with trace zero. Note that

$$\begin{aligned}
\nabla u_1 \cdot \nabla u_2 &= (i\pi k + \pi a)u_1 \cdot (i\pi k - \pi a)u_2 \\
&= (-\pi^2|k|^2 - \pi^2|a|^2)\exp\left[2\pi i x \cdot k\right] \\
&= -2\pi^2|k|^2 \exp\left[2\pi i x \cdot k\right].
\end{aligned}$$

Then,

$$\begin{aligned}
\int_{\partial\Omega} \psi_1(\Lambda_\gamma - \Lambda_1)\psi_2 \mathrm{d}s(x) &= \int_{\partial\Omega} \left(w_1 \gamma \frac{\partial \omega_2}{\partial \nu} - u_1 \frac{\partial u_2}{\partial \nu} \right) \mathrm{d}s(x) \\
&= \int_\Omega \left(\gamma \nabla\omega_1 \cdot \nabla\omega_2 - \nabla u_1 \cdot \nabla u_2 \right) \mathrm{d}x \\
&= \int_\Omega \left\{ \delta(\nabla u_1 \cdot \nabla u_2 + \nabla u_1 \cdot \nabla v_2 + \nabla v_1 \cdot \nabla u_2) + \gamma \nabla v_1 \cdot \nabla v_2 \right\} \mathrm{d}x \\
&= -2\pi^2|k|^2 \int_\Omega \delta(x) \exp\left[2\pi i k \cdot x\right] \mathrm{d}x + \tilde{R}(k),
\end{aligned}$$

where $\tilde{R}(k)$ is the last three terms in the third line of equation above. Dividing the first line and the last line in the above equations by $-2\pi^2|k|^2$, we get

$$\int_\Omega \delta(x)\exp\left[2\pi i x\cdot k\right]\mathrm{d}x = -\frac{1}{2\pi^2|k|^2}\int_{\partial\Omega}\psi_1(\Lambda_\gamma-\Lambda_1)\psi_2\mathrm{d}s(x) + \frac{\tilde{R}(k)}{2\pi^2|k|^2},$$

of which the left term is the Fourier transform of $\delta(x)$. We denote the Fourier transform of $\delta(x)$ by $\hat{\delta}(k)$, the first term on the right-hand side equation by $\hat{F}(k)$, and the last term by $\hat{R}(k)$. Calderón showed that $R(x)$, which is the inverse Fourier transform of $\hat{R}(k)\hat{\eta}(k)$, where $\hat{\eta}(k)$ is a Gaussian low pass filter, is negligible provided that $\|\delta\|_\infty$ is small. In this paper, instead of multiplying by $\hat{\eta}(k)$, we truncate the $\hat{F}(k)$ to a sphere of radius R_T, and adopt the notation $\hat{F}_{R_T}(k)$. This has the regularizing effect of smoothing the reconstruction; decreasing R_T results in increased smoothing. Therefore, by neglecting $\hat{R}(k)$ and taking the inverse Fourier transform of the truncated $\hat{F}_{R_T}(k)$, we get an approximation of the perturbation $\delta(x)$ by

$$\delta(x) \approx \mathcal{F}^{-1}\left(\hat{F}_{R_T}(k)\right)(x). \tag{4.10}$$

4.3 Computational considerations

For functions f and g of θ and z such that $f, g : \mathbb{R}^K \times \mathbb{R}^J \to \mathbb{C}$, let $(f(\cdot,\cdot), g(\cdot,\cdot))_L$ denote the discrete bilinear form defined by

$$(f(\cdot,\cdot), g(\cdot,\cdot))_L = \sum_{l_z=1}^{J}\sum_{l=1}^{K} f(\theta_l, z_{l_z})g(\theta_l, z_{l_z}).$$

We expand ψ_1 and ψ_2 on the boundary $\partial\Omega$ with respect to I^i_{l,l_z} and $U^{i,\gamma}_{l,l_z}$ by letting

$$\psi_1(\theta_l, z_{l_z}; k) = \sum_{i}^{L-1} a^i_k I^i_{l,l_z}, \tag{4.11}$$

$$\psi_2(\theta_l, z_{l_z}; k) = \sum_{j}^{L-1} b^j_{k,\gamma} U^{j,\gamma}_{l,l_z}, \tag{4.12}$$

neglecting the constant terms in the expansion since they will be annihilated by Λ_γ in the expansion of the integral. Since the current patterns $\{I^i\}_{i=1}^{L-1}$ are orthonormal, we can solve (4.11) for $\mathbf{a}_k = \{a_k^i\}_{i=1}^{L-1}$ by

$$a_k^i = (\psi_1, I^i)_L.$$

On the other hand, taking the inner product with $U^{i,\gamma}$ on both sides of (4.12), we get

$$\sum_{j=1}^{L-1} b_{k,\gamma}^j (U^{i,\gamma}, U^{j,\gamma})_L = (\psi_2, U^{i,\gamma})_L,$$

for $i = 1, \ldots, L-1$. Therefore, we get a system of linear equations for $\mathbf{b}_{k,\gamma} = \left\{b_{k,\gamma}^j\right\}_{j=1}^{L-1}$ in a matrix form:

$$\mathbf{U}_\gamma \mathbf{b}_{k,\gamma} = \mathbf{c}_{k,\gamma},$$

where $\mathbf{U}_\gamma(i,j) = (U^{i,\gamma}, U^{j,\gamma})_L$ and $c_{k,\gamma}^i = (\psi_2, U^{i,\gamma})_L$. Since $\mathbf{U}_\gamma$ is invertible, we get

$$\mathbf{b}_k = (\mathbf{U}_\gamma)^{-1} \mathbf{c}_{k,\gamma}.$$

Now, with (4.11) and (4.12),

$$\begin{aligned}
\int_{\partial\Omega} \psi_1 \Lambda_\gamma \psi_2 \mathrm{d}s(x) &= \int_{\partial\Omega} \sum_{i=1}^{L-1} a_k^i I^i \Lambda_\gamma \sum_{j=1}^{L-1} b_{k,\gamma}^j U^{j,\gamma} \mathrm{d}s(x) \\
&= A \sum_{i=1}^{L-1} \sum_{j=1}^{L-1} a_k^i b_{k,\gamma}^j \left(I_{l,l_z}^i, \left[\Lambda_\gamma U^{j,\gamma}\right]_{l,l_z} \right)_L \\
&\approx \sum_{i=1}^{L-1} \sum_{j=1}^{L-1} a_k^i b_{k,\gamma}^j \left(I_{l,l_z}^i, I_{l,l_z}^j \right)_L,
\end{aligned}$$

where A is the area of the electrodes. Note that in the ideal case, $\Lambda_\gamma u|_{\partial\Omega} = j(x)$, but in the discrete case with the CEM, it is an approximation to take $\Lambda_\gamma U^{j,\gamma} \approx I_{l,l_z}^j$. Defining the matrix

$\mathbf{T} \in \mathbb{R}^{L-1,L-1}$ by $\mathbf{T}(i,j) = \left(I^i_{l,l_z}, I^j_{l,l_z}\right)_L$, we get

$$\int_{\partial\Omega} \psi_1 \Lambda_\gamma \psi_2 ds(x) = \mathbf{a}_k^t \mathbf{T} \mathbf{b}_{k,\gamma}.$$

Therefore, we approximate $\hat{F}_{R_T}(k)$ by

$$\hat{F}_{R_T}(k) = -\frac{1}{2\pi^2|k|^2} \mathbf{a}_k^t \mathbf{T}(\mathbf{b}_{k,\gamma} - \mathbf{b}_{k,1}). \tag{4.13}$$

For the computation of the inverse Fourier transform, we use the Simpson's quadrature rule. Note that the computation of $\delta(x)$ is trivially parallelizable in x since the reconstruction is computed independently for each value of x by invering (4.13).

4.4 Numerical results

In this section, reconstructions using Calderón's method for simulated and experimental data in the cylindrical geometry are presented. Reconstructions from data on a tank with two rows and four rows of electrodes with targets at various vertical locations demonstrate the resolution of the method in the z-direction. Reconstructions from data collected on a saline-filled tank demonstrate that the method is effective in the presence of actual noise.

4.4.1 Forward model simulation

Data was simulated with the FEM for a cylindrical tank of radius 8 cm, and height 18.53 cm with 2 and 4 rows of 2.54 cm by 2.54 cm electrodes around the circumference. In the case of two rows of electrodes, the first layer of electrodes is centered at height $z_1 = 7.57$ cm, and the second layer at height $z_2 = 10.96$ cm. For the case of four layers of electrodes, two layers of electrodes are added above and below those of the two layer case at heights $z_4 = 14.35$ cm and $z_1 = 4.18$ cm, respectively. The vertical gap between two adjacent rows of electrodes is 0.85 cm. Voltage measurements at the electrodes were simulated using the FEM on a mesh of 205,120 tetrahedrons and 38,529 nodes for the case of 2 layers of electrodes and 221,416 tetrahedrons, 41,362 nodes for the case of 4 layers of electrodes. Gaussian noise was added to the simulated data independently for each current pattern according to the formula

$$U^{j}_{a,\gamma} = U^{j,\gamma} + \frac{a}{100}||U^{j,\gamma}||_{\infty}Z,$$

where $U^{j,\gamma}_{a}$ is the noisy data with noise level $a\%$, $U^{j,\gamma}$ is the simulated data and Z is the standard multivariate normal random variable. In each example, the conductivity of the background was 1.8 mS/cm, and the contact impedance was $z_l = 1.3$ Ohm-cm^2. The conductivities of the targets were 6 mS/cm and 0.5 mS/cm.

4.4.2 3D reconstruction examples

Reconstructions from simulated data with two rows and four rows are compared, demonstrating the method's ability to locate a target in the plane of the electrodes and the resolution in x, y, and z. In each example, the displayed reconstructions are the perturbations $\delta(x)$, while the displayed ground truth is $\gamma(x)$. Reconstructions from data with and without noise are shown to illustrate the effect of noise on the resolution. Finally, the method is demonstrated on tank data collected on a 3D tank with two layers of electrodes. In the figures, 3D rendered images are included composed of 20 reconstructed slices that extend 1 cm above and 1 cm below the top and bottom rows of electrodes, respectively.

Simulated data with 2 electrode layers

Figure 4.1 shows the reconstructions of $\delta(x)$ for one conductor located in the plane of the bottom row of electrodes, and Figure 4.2 shows reconstructions for one conductor located just above the plane of the top layer of electrodes. In both figures, the ground truth and the 3D image of the target configuration are depicted in the first row. Throughout all figures, bars with ticks represent the vertical locations of the centers of electrodes layers and the arrow represents the height of the reconstructed slice depicted in the figure. The first column of reconstructions are from noise-free data, while the second column is from data with 0.1% additive noise. The truncation radius in

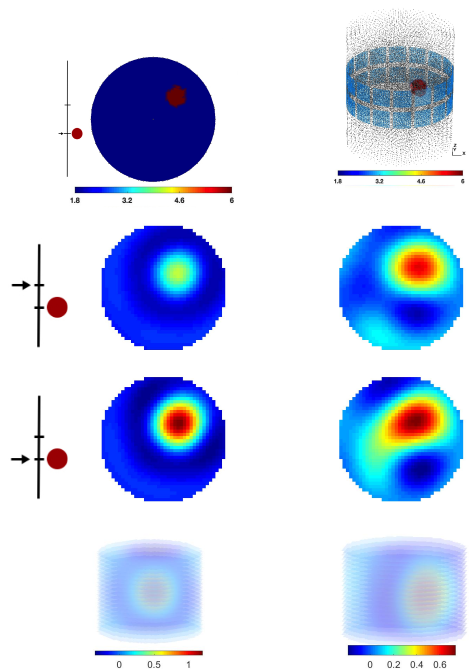

Figure 4.1: Reconstructions for simulated data with two electrode layers. Top row: Ground truth, a spherical conductive target of diameter 2.5 cm. First column of reconstructions: Reconstructions from noise-free data of one conductor located at the height of the bottom layer of electrodes. The truncation radius is 17. Second column of reconstructions: Reconstructions from data with 0.1% additive noise. The truncation radius is 14. The arrow indicates the height of the reconstructed slice displayed. Last row is the 3D rendering of 20 reconstructed slices that extend 1 cm above and 1 cm below the top and bottom rows of electrodes, respectively, for the corresponding columns.

formula (4.10) is 17 for noise-free data and 14 for noisy data. The last row of the figures contains 3D rendering of 20 slices of images starting from 1 cm below the bottom layer of electrodes to 1 cm above the top layer of electrodes.

Figures 4.1 and 4.2 demonstrate that an out-of-plane target is visible in the reconstruction, as predicted and demonstrated in [9]. The resolution in both x, y and the z-axis is seen to be negatively influenced in the presence of noise.

Simulated data with 4 layers of electrodes

Figure 4.3 shows reconstructions of $\delta(x)$ from simulated data with one conductor and one resistive target at the heights of the third and second electrode layers, respectively. The first column of reconstructions are from noise-free data, while the second column is from data with 0.1% additive noise. The truncation radius in formula (4.10) is 17 for noise-free data and 14 for noisy data.

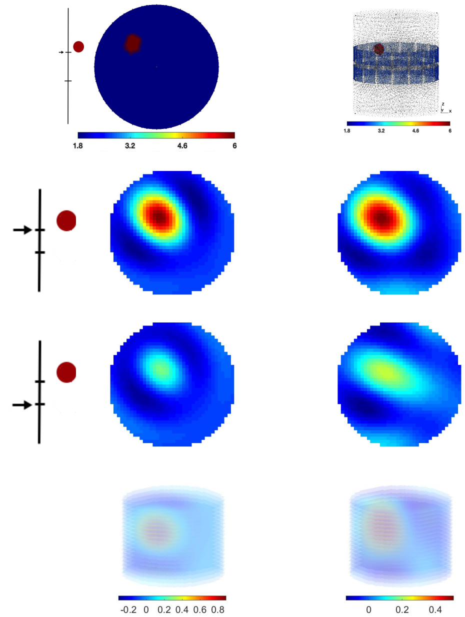

Figure 4.2: Reconstructions for simulated data with 2 electrode layers. Top row: Ground truth, a spherical conductive target of diameter 2.5 cm. First column of reconstructions: Reconstructions from noise-free data of one conductor located just above the top layer of electrodes. The truncation radius is 17. Second column of reconstructions: Reconstructions from data with 0.1% additive noise. The truncation radius is 14. The arrow indicates the height of the reconstructed slice displayed. Last row is the 3D rendering of 20 reconstructed slices that extend 1 cm above and 1 cm below the top and bottom rows of electrodes, respectively, for the corresponding columns.

In order to demonstrate the vertical resolution of the 3D algorithm, we consider reconstructions of a dynamic target located at each of the four electrode layers. Reconstructions from noise-free and data with 0.05% additive noise are found in Figures 4.4 and 4.5. The truncation radius in formula (4.10) is 17 for noise-free data and 15 for noisy data. Last row is the 3D rendering of 20 reconstructed slices that extend 1 cm above and 1 cm below the top and bottom rows of electrodes, respectively, for the corresponding columns. While there are some artefacts in the layers with no target, the z-resolution is quite good in the noise-free case and deteriorates somewhat in the presence of noise.

Experimental tank data with two layers of electrodes

Data was collected on a saline-filled tank of radius 15 cm using the ACE 1 EIT system [52]. The tank was constructed with two layers of electrodes with 32 electrodes per layer, but since ACE

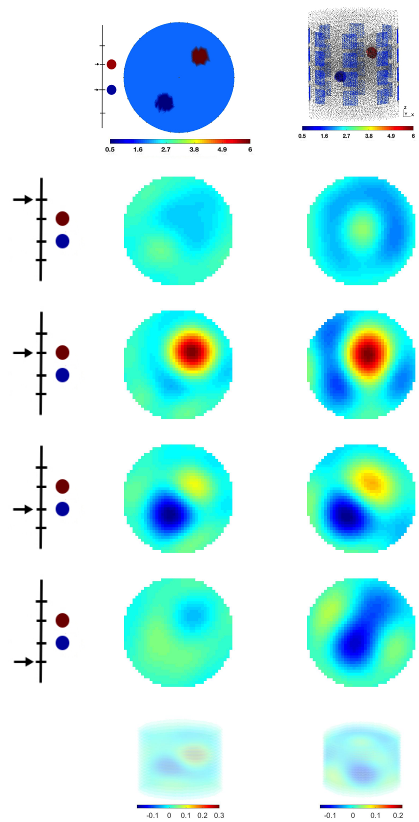

Figure 4.3: Reconstructions for simulated data with 4 layers of electrodes each layer having 8 electrodes uniformly spaced. Top row: Ground truth, a spherical conductive target of diameter 2.44 cm and a resistive target of diameter 2.6 cm. First column of reconstructions: Reconstruction from noise free data of one conductor located at the height of second top layer of electrodes and one insulator located at the height of second bottom layer of electrodes. The truncation radius is 17. Second column: Reconstructions for the 0.1% noise data with the same target configuration. The truncation radius is 14. The arrow indicates the height of the reconstructed slice displayed. Last row is the 3D rendering of 20 reconstructed slices that extend 1 cm above and 1 cm below the top and bottom rows of electrodes, respectively, for the corresponding columns.

1 has 32 channels, every second electrode in the layer was used for voltage measurement. ACE 1 is a bipolar active electrode system that applies current pairwise at 125 kHz on up to 32 electrodes and measures the resulting voltages on all electrodes. Adjacent current patterns with amplitude 3.3276 mA were applied on the electrodes connected to the system and voltages were measured while a plastic ball 3 cm in diameter placed at the height of the center of the two layers was moved counter-clockwise around the tank. Reconstructions of $\delta(x)$ at four time snapshots are found in Figure 4.6.

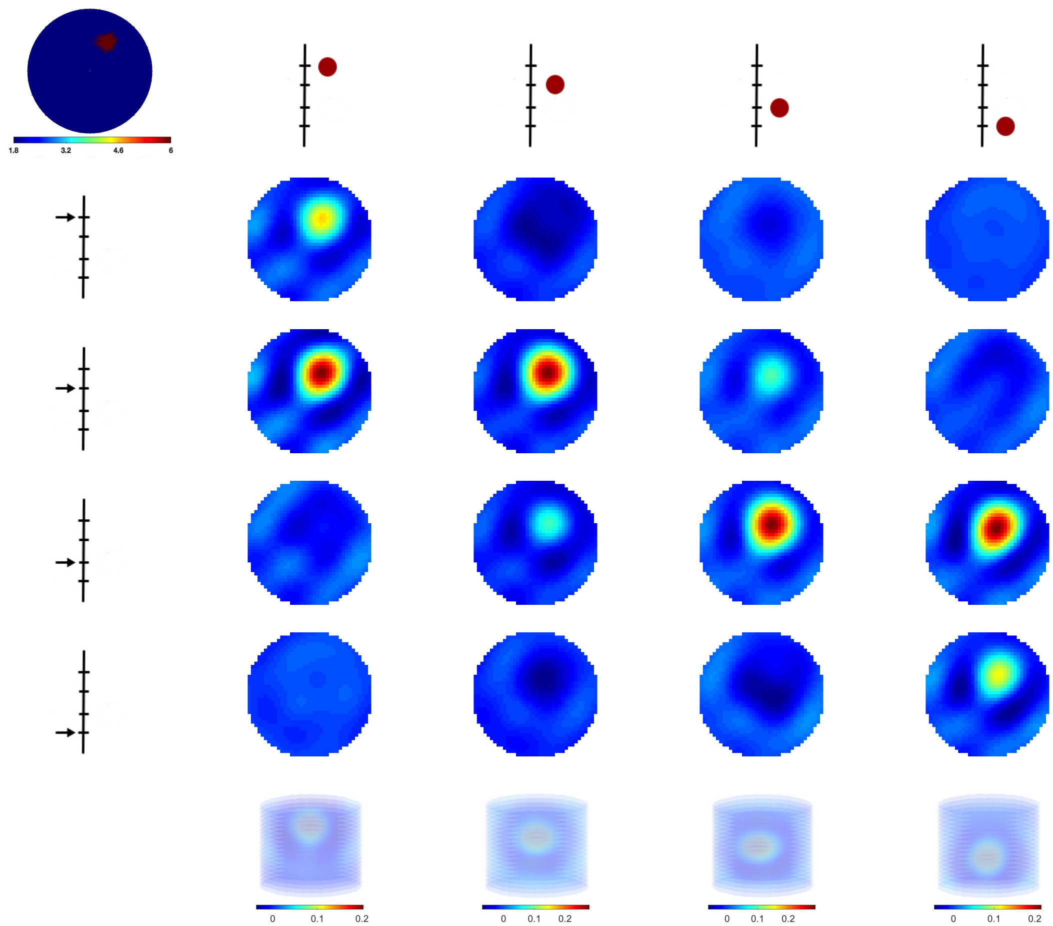

Figure 4.4: Reconstructions from noise-free simulated data for four different vertical locations of the target with 4 layers of electrodes each layer having 8 electrodes uniformly spaced. The first row shows the ground truth, a spherical conductive target of diameter 2.5 cm, and the vertical location of the conductor, for the corresponding columns, with respect to the electrode layers. From the second column to the last column, the target is located at different heights indicated in the first row. From the second row to the fifth row, the images show the reconstructions taken at different heights described by the arrow in the first column. Last row is the 3D rendering of 20 reconstructed slices that extend 1 cm above and 1 cm below the top and bottom rows of electrodes, respectively, for the corresponding columns. The truncation radius is 17 for all figures.

4.5 Conclusions

In summary, we have presented an implementation of Calderón's method in three dimensions with measurements on a portion of a cylindrical domain. The method has the advantage of being trivially parallelizable, and able to compute reconstructions voxel-wise in a region of interest. Results from simulated and experimental data show that the method is effective for distinguishing

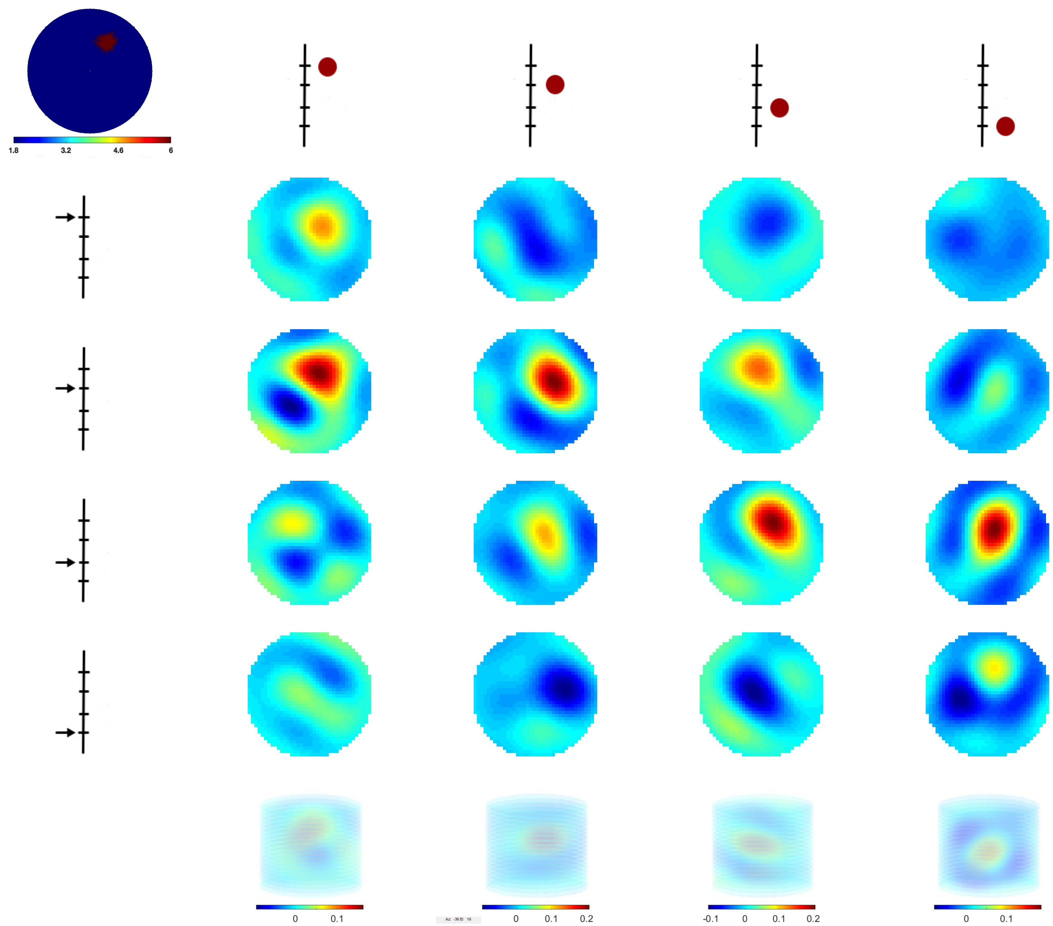

Figure 4.5: Reconstructions for four different vertical locations of the target with 4 layers of electrode configuration with 0.05 % noise added to the data. The configuration of the figures is the same as Fig. 4.4. The truncation radius is 15 for all figures.

in-plane and nearby out-of-plane inhomogeneities with good spatial resolution in the vertical z direction. A study of the sensitivity to modeling errors and a comparison to other methods is a topic of future work.

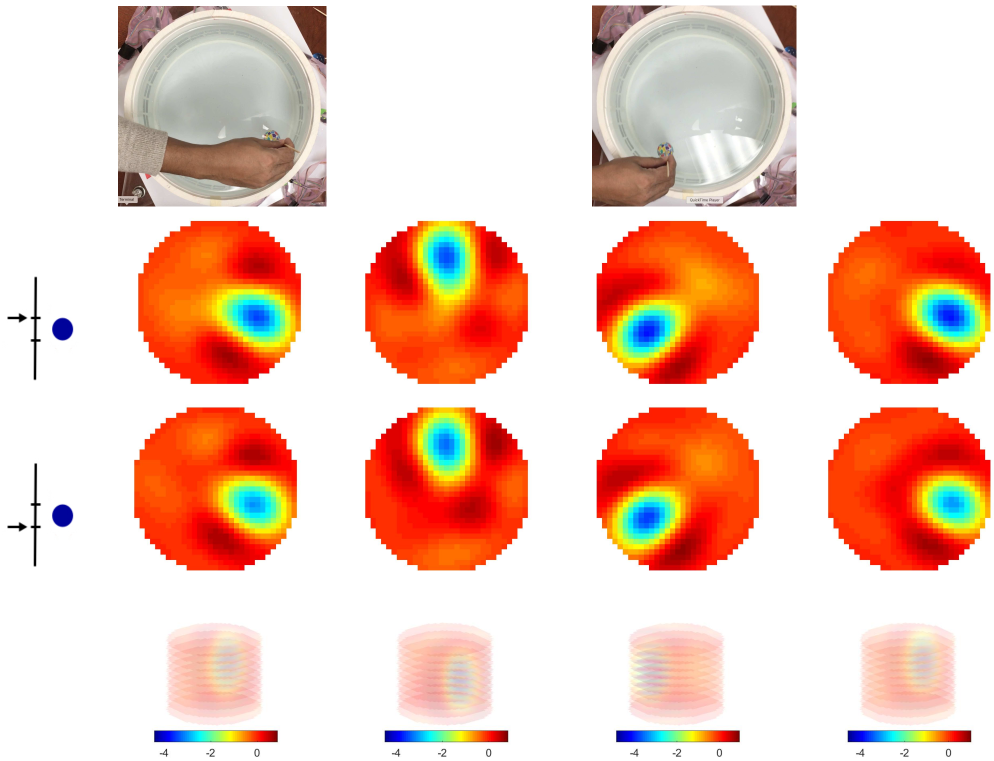

Figure 4.6: Reconstructions from tank data with a plastic ball 3 cm in diameter moving counter-clockwise at a height between the middle of the two electrodes layers. The first row of images shows the top slice and the second row of images shows the bottom slices, and the third row is the 3D rendering of 10 reconstructed slices starting 1 cm below the bottom layer to 1 cm above the top layer.

Chapter 5

Conclusions

In this dissertation, we presented three papers about two and three dimensional Calderón's method. In the first paper, we presented a second order Calderón's method suggested from the study of its relationship to the D-bar method. We verified that the second order term that we suggest is dominating the other second order terms that we are dropping. We also claim that the second order strategy is applicable to the complex admittivity targets by testing the algorithm to simulated data and experimental data. We also developed a method of including a spatial *a priori* information to Calderón's method. The results with experimental tank data show that the second order term and the inclusion of a spatial prior improves the reconstruction over the original Calderón's method. We used the SSIM measures to support our claim. Approximating CGO solutions $\psi(x,k)$ and the integral equation for $\mu(x,k)$ by using the Born series is a topic of future work. In the second paper, we proposed a new kind of expansion for the given harmonic functions. To this end, we first extracted the locations of the electrodes and then computed the harmonic functions at those locations. Then, we expanded the harmonic functions at the location of electrodes by the measured voltages and the applied current patterns. With this new strategy, we were able to include the location of electrodes to Calderón's method. We demonstrated that including the location of electrodes improves the absolute image significantly. The difference image with our method is no worse than the original Calderón's method. This method is easy to understand, direct, and can be applied to more general experimental settings such as three-dimensional arbitrary domain shape. An implementation of this method to data with different geometry including human subject data is a topic of future work. In the third paper, we presented an implementation of Calderón's method on the cylindrical geometry with multiple layers of electrodes. In order to test our algorithm, we generated simulated data by solving the forward problem by the Finite Element Method. Then, by using the simulated data with two or four layers of electrodes, we showed that the method is effective for locating the targets with good spatial resolution. We also tested our algorithm with cylinder tank data and showed that the method captures the dynamic changes of the subject effectively. A study on various three-dimensional geometry and electrode configurations is a topic of future work. Comparing this method with other three dimensional EIT algorithms is another topic of future work.

Bibliography

[1] G. Alessandrini. Stable determination of conductivity by boundary measurements. *Applicable Analysis*, 27:153–172, 01 1988.

[2] M. Alsaker. *Computational Advancements in the D-bar Reconstruction Method for 2-D Electrical Impedance Tomography*. PhD thesis, USA, 2006.

[3] M. Alsaker, S. Hamilton, and A. Hauptmann. A direct d-bar method for partial boundary data electrical impedance tomography with a priori information. *Inverse Problems and Imaging*, 11:427–454, 04 2017.

[4] M. Alsaker and J. Mueller. A d-bar algorithm with a priori information for electrical impedance tomography. *SIAM Journal on Imaging Sciences*, 9, 05 2015.

[5] M. Alsaker and J. Mueller. Use of an optimized spatial prior in d-bar reconstructions of eit tank data. *Inverse Problems and Imaging*, 12:883–901, 08 2018.

[6] N. Avis and D. Barber. Incorporating a priori information into the sheffield filtered backprojection algorithm. *Physiological measurement*, 16:A111–22, 09 1995.

[7] U. Baysal and B. Eyüboğlu. Use of a priori information in estimating tissue resistivities - a simulation study. *Physics in medicine and biology*, 43:3589–606, 01 1999.

[8] J. Bikowski and J. L. Mueller. 2D EIT reconstructions using Calderon's method. *Inverse Problems and Imaging*, 2(1):43–61, 2008.

[9] N. J. Blue RS, Isaacson D. *Real-Time Three-Dimensional Electrical impedance Tomography*. PhD thesis, Troy, NY, USA, 1997. AAI9120220.

[10] G. Boverman, T.-J. Kao, D. Isaacson, and G. Saulnier. An implementation of calderón's method for 3-d limited-view eit. *IEEE transactions on medical imaging*, 28:1073–82, 02 2009.

[11] B. Brown. Electrical impedance tomography (eit): A review. *Journal of medical engineering & technology*, 27:97–108, 05 2003.

[12] A. Calderón. On inverse boundary value problem. *Computational & Applied Mathematics - COMPUT APPL MATH*, 25, 01 2006.

[13] D. L. B. Camargo, E. *Desenvolvimento de algoritmo de imagens absolutas de Tomografia por Impedância Elétrica para uso clínico*. PhD thesis, 2013.

[14] Z. Cao and L. Xu. Direct recovery of the electrical admittivities in 2d electrical tomography by using calderon's method and two-terminal/electrode excitation strategies. *Measurement Science and Technology*, 24:074007, 07 2013.

[15] Z. Cao, L. Xu, and H. Wang. Image reconstruction technique of electrical capacitance tomography for low-contrast dielectrics using calderon's method. *Measurement Science and Technology*, 20:104027, 09 2009.

[16] M. Cheney, D. Isaacson, J. Newell, S. Simske, and J. Goble. Noser: An algorithm for solving the inverse conductivity problem. *International Journal of Imaging Systems & Technology*, 2:66–75, 06 1990.

[17] M. Cheney, E. Somersaalo, and D. Isaacson. Existence and uniqueness for electrode models for electric current computed tomography. *Siam Journal on Applied Mathematics - SIAMAM*, 52, 01 1991.

[18] K.-S. Cheng, D. ISAACSON, J. Newell, and D. GISSER. Electrode models for electric current computed tomography. *IEEE transactions on bio-medical engineering*, 36:918–24, 10 1989.

[19] V. Cherepenin, A. Karpov, A. Korjenevsky, V. Kornienko, A. Mazaletskaya, D. Mazourov, and D. Meister. A 3d electrical impedance tomography (eit) system for breast cancer detection. *Physiological measurement*, 22:9–18, 03 2001.

[20] M. Choi, T.-J. Kao, D. Isaacson, G. Saulnier, and J. Newell. A reconstruction algorithm for breast cancer imaging with electrical impedance tomography in mammography geometry. *Biomedical Engineering, IEEE Transactions on*, 54:700 – 710, 05 2007.

[21] H. Dehghani, D. Barber, and I. Basarab-Horwath. Incorporating a priori anatomical information into image reconstruction in electrical impedance tomography. *Physiological measurement*, 20:87–102, 03 1999.

[22] D. Dobson and F. Santosa. An image-enhancement technique for electrical impedance. *Inverse Problems*, 10:317, 01 1999.

[23] B. Eyüboğlu, B. Brown, and D. Barber. Limitations to sv determination from apt images. pages 442 – 443 vol.2, 12 1989.

[24] D. Ferrario, B. Grychtol, A. Adler, J. Solà, S. Bohm, and M. Bodenstein. Toward morphological thoracic eit: Major signal sources correspond to respective organ locations in ct. *IEEE transactions on bio-medical engineering*, 59:3000–8, 07 2012.

[25] D. Ferrario, B. Grychtol, A. Adler, J. Solà, S. Bohm, and M. Bodenstein. Toward morphological thoracic eit: Major signal sources correspond to respective organ locations in ct. *IEEE transactions on bio-medical engineering*, 59:3000–8, 07 2012.

[26] D. Flores-Tapia and S. Pistorius. Electrical impedance tomography reconstruction using a monotonicity approach based on a priori knowledge. *Conference proceedings : ... Annual International Conference of the IEEE Engineering in Medicine and Biology Society. IEEE Engineering in Medicine and Biology Society. Conference*, 2010:4996–9, 08 2010.

[27] E. Francini. Recovering a complex coefficient in a planar domain from the dirichlet-to-neumann map. *Inverse Problems*, 16:107, 01 2000.

[28] I. Frerichs, M. Amato, A. Kaam, D. Tingay, Z. Zhao, B. Grychtol, M. Bodenstein, H. Gagnon, S. Bohm, E. Teschner, O. Stenqvist, T. Mauri, V. Torsani, L. Camporota, A. Schibler, G. Wolf,

D. Gommers, S. Leonhardt, and A. Adler. Chest electrical impedance tomography examination, data analysis, terminology, clinical use and recommendations: consensus statement of the translational eit development study group. *Thorax*, 72:83–93, 09 2016.

[29] I. Frerichs, G. Elke, S. Pulletz, D. Schaedler, G. Zick, J. Scholz, and N. Weiler. Reproducibility of regional lung ventilation distribution determined by electrical impedance tomography during mechanical ventilation. *Physiological measurement*, 28:S261–7, 08 2007.

[30] I. Frerichs, J. Hinz, P. Herrmann, G. Weisser, G. Hahn, T. Dudykevych, M. Quintel, and G. Hellige. Detection of local lung air content by electrical impedance tomography compared with electron beam ct. *Journal of applied physiology (Bethesda, Md. : 1985)*, 93:660–6, 09 2002.

[31] I. Frerichs, S. Pulletz, G. Elke, F. Reifferscheid, D. Schaedler, J. Scholz, and N. Weiler. Assessment of changes in distribution of lung perfusion by electrical impedance tomography. *Respiration; international review of thoracic diseases*, 77:282–91, 02 2009.

[32] L. Fuks, M. Cheney, D. Isaacson, D. Gisser, and J. Newell. Detection and imaging of electric conductivity and permittivity at low frequency. *IEEE transactions on bio-medical engineering*, 38:1106–10, 12 1991.

[33] J. C. Goble. *The Three-Dimensional Inverse Problem in Electric Current Computed Tomography*. PhD thesis, USA, 1990. AAI9120220.

[34] B. Grychtol, B. Müller, and A. Adler. 3d eit image reconstruction with greit. *Physiological Measurement*, 37:785–800, 06 2016.

[35] R. Guardo, C. Boulay, B. Murray, and M. Bertrand. An experimental study in electrical impedance tomography using backprojection reconstruction. *IEEE transactions on biomedical engineering*, 38:617–27, 08 1991.

[36] S. Hamilton, C. Herrera, J. Mueller, and A. Herrmann. A direct d-bar reconstruction algorithm for recovering a complex conductivity in 2d. *Inverse problems*, 28, 07 2012.

[37] C. Herrera, M. Vallejo, J. Mueller, and R. Lima. Direct 2-d reconstructions of conductivity and permittivity from eit data on a human chest. *IEEE transactions on medical imaging*, 34, 09 2014.

[38] T. Hope and S. Iles. Technology review: The use of electrical impedance scanning in the detection of breast cancer. *Breast cancer research : BCR*, 6:69–74, 02 2004.

[39] D. Isaacson, J. Mueller, J. Newell, and S. Siltanen. Reconstructions of chest phantoms by the d-bar method for electrical impedance tomography. *IEEE transactions on medical imaging*, 23:821–8, 08 2004.

[40] D. Isaacson, J. Newell, J. Goble, and M. Cheney. Thoracic impedance images during ventilation. pages 106 – 107, 12 1990.

[41] F. Joel, S. Mikko, and U. Gunther. The calderón's problem - an introduction to inverse problems. *Textbook in progress*.

[42] J. Jordana, M. Gasulla, and R. Pallas-Areny. Electrical resistance tomography to detect leaks from buried pipes. *Measurement Science and Technology*, 12:1061, 07 2001.

[43] J. Jossinet. Variability of impedivity in normal and pathological breast tissue. *Medical & biological engineering & computing*, 34:346–50, 09 1996.

[44] J. Jossinet. The impedivity of freshly excised human breast tissue. *Physiological measurement*, 19:61–75, 02 1998.

[45] T.-J. Kao, D. Isaacson, J. Newell, and G. Saulnier. A 3d reconstruction algorithm for eit using a handheld probe for breast cancer detection. *Physiological measurement*, 27:S1–11, 06 2006.

[46] M. Knudsen, K. andLassas, J. L. Mueller, and S. Siltanen. D-bar method for electrical impedance tomography with discontinuous conductivities. *SIAM Journal on Applied Mathematics*, 67(3):893–913, 2007.

[47] V. Kolehmainen, M. Vauhkonen, P. Karjalainen, and J. Kaipio. Assessment of errors in static electrical impedance tomography with adjacent and trigonometric current patterns. *Physiological measurement*, 18:289–303, 12 1997.

[48] G. Lytle, P. Perry, and S. Siltanen. Nachman's reconstruction method for the calderon problem with discontinuous conductivities. *Inverse Problems*, 36, 11 2019.

[49] T. Martins, A. Sato, F. Moura, E. Camargo, O. Silva, T. Santos, Z. Zhao, K. Möeller, M. Amato, J. Mueller, R. Lima, and M. Tsuzuki. A review of electrical impedance tomography in lung applications: Theory and algorithms for absolute images. *Annual Reviews in Control*, 48, 05 2019.

[50] A.-Z. Mehrnoosh and L. Latiff. Electrical impedance tomography as a primary screening technique for breast cancer detection. *Asian Pacific journal of cancer prevention : APJCP*, 16:5595–7, 08 2015.

[51] M. Mellenthin, J. Mueller, E. Camargo, F. Moura, S. Hamilton, and R. Lima. The ace1 thoracic electrical impedance tomography system for ventilation and perfusion. pages 4073–4076, 08 2015.

[52] M. Mellenthin, J. Mueller, E. Camargo, F. Moura, T. Santos, R. Lima, S. Hamilton, P. Muller, and M. Alsaker. The ace1 electrical impedance tomography system for thoracic imaging. *IEEE Transactions on Instrumentation and Measurement*, PP:1–14, 11 2018.

[53] J. Mueller, D. Isaacson, and J. Newell. A reconstruction algorithm for electrical impedance tomography data collected on rectangular electrode arrays. *IEEE transactions on bio-medical engineering*, 46:1379–86, 12 1999.

[54] J. Mueller and S. Siltanen. Direct reconstructions of conductivities from boundary measurements. *Siam Journal on Scientific Computing*, 24, 01 2003.

[55] J. Mueller and S. Siltanen. Linear and nonlinear inverse problems with practical applications. 06 2020.

[56] P. Muller, D. Isaacson, J. Newell, and G. Saulnier. Calderon's method on an elliptical domain. *Physiological measurement*, 34:609–622, 06 2013.

[57] P. Muller and J. Mueller. Reconstruction of complex conductivities by calderon's method on subject-specific domains. pages 1–2, 03 2018.

[58] P. Muller, J. Mueller, and M. Mellenthin. Real-time implementation of calderón's method on subject-specific domains. *IEEE Transactions on Medical Imaging*, PP:1–1, 04 2017.

[59] M. Music and P. Perry. Global solutions for the zero-energy novikov–veselov equation by inverse scattering. *Nonlinearity*, 31, 02 2015.

[60] A. Nachman. Global uniqueness for a two-dimensional inverse boundary value problem. *Annals of Mathematics. Second Series*, 143, 01 1996.

[61] D. T. Nguyen, C. Jin, A. Thiagalingam, and A. Mcewan. A review on electrical impedance tomography for pulmonary perfusion imaging. *Physiological measurement*, 33:695–706, 04 2012.

[62] A. Nissinen, L. Heikkinen, V. Kolehmainen, and J. Kaipio. Compensation of errors due to discretization, domain truncation and unknown contact impedances in electrical impedance tomography. *Measurement Science and Technology*, 20:105504, 09 2009.

[63] A. Noordegraaf, T. Faes, A. Janse, J. Marcus, J. Bronzwaer, P. Postmus, and P. Vries. Noninvasive assessment of right ventricular diastolic function by electrical impedance tomography. *Chest*, 111:1222–8, 06 1997.

[64] A. Noordegraaf, T. Faes, J. Marcus, A. Janse, R. Heethaar, P. Postmus, and P. Vries. Improvement of cardiac imaging in electrical impedance tomography by means of a new electrode configuration. *Physiological measurement*, 17:179–88, 09 1996.

[65] K. S. Rabbani and A. M. B. H. Kabir. Studies on the effect of the third dimension on a two-dimensional electrical impedance tomography system. *Clinical Physics and Physiological Measurement*, 12(4):393–402, nov 1991.

[66] O. Raneta, D. Ondrus, and V. Bella. Utilisation of electrical impedance tomography in breast cancer diagnosis. *Klinická onkologie : casopis Ceské a Slovenské onkologické spolecnosti*, 25:36–41, 01 2012.

[67] G. Saulnier, N. Liu, C. Tamma, H. Xia, T.-J. Kao, J. Newell, and D. Isaacson. An electrical impedance spectroscopy system for breast cancer detection. *Conference proceedings : ... Annual International Conference of the IEEE Engineering in Medicine and Biology Society. IEEE Engineering in Medicine and Biology Society. Conference*, 2007:4154–7, 02 2007.

[68] S. Siltanen, J. Mueller, and D. Isaacson. An implementation of the reconstruction algorithm of a nachman for the 2d inverse conductivity problem. *Inverse Problems*, 16:681, 06 2000.

[69] B. Singh, C. Smith, and R. Hughes. In vivo dielectric spectrometer. *Medical & biological engineering & computing*, 17:45–60, 02 1979.

[70] H. Smit, A. Noordegraaf, J. Marcus, A. Boonstra, P. Vries, and P. Postmus. Determinants of pulmonary perfusion measured by electrical impedance tomography. *European journal of applied physiology*, 92:45–9, 06 2004.

[71] M. Soleimani. Electrical impedance tomography imaging using a priori ultrasound data. *Biomedical engineering online*, 5:8, 02 2006.

[72] G. Steiner, M. Soleimani, and D. Watzenig. A bio-electromechanical imaging technique with combined electrical impedance and ultrasound tomography. *Physiological measurement*, 29:S63–75, 07 2008.

[73] A. Surowiec, S. Stuchly, J. Barr, and A. Swarup. Electrical properties of breast carcinoma and surrounding tissues. *IEEE transactions on bio-medical engineering*, 35:257–63, 05 1988.

[74] J. Sylvester. A uniqueness theorem for an inverse boundary value problem in electrical prospection. *Communications on Pure and Applied Mathematics*, 39:91 – 112, 01 1986.

[75] J. Sylvester. A global uniqueness theorem for an inverse boundary value problem. *Annals of Mathematics. Second Series*, 125, 01 1987.

[76] G. Ulhman. Electrical impedance tomography and calderón's problem. *Inverse Problems*, 25, 12 2009.

[77] G. Ulhman. Inside out: Inverse problems and applications. reprint of the 2003 hardback ed. 06 2020.

[78] M. Vauhkonen, D. Vadász, P. Karjalainen, E. Somersalo, and J. Kaipio. Tikhonov regularization and prior information in electrical impedance tomography. *IEEE transactions on medical imaging*, 17:285–93, 05 1998.

[79] P. Vauhkonen, M. Vauhkonen, T. Savolainen, and J. Kaipio. Three-dimensional electrical impedance tomography based on the complete electrode model. *IEEE transactions on biomedical engineering*, 46:1150–60, 10 1999.

[80] P. J. Vauhkonen. *Image Reconstruction in Three-Dimensional Electrical Impedance Tomography*. PhD thesis, 2004.

[81] J. Victorino, J. Borges, V. Okamoto, G. Matos, M. Tucci, M. Caramez, H. Tanaka, F. Suarez-Sipmann, D. Santos, C. Barbas, C. Carvalho, and M. Amato. Imbalances in regional lung ventilation: A validation study on electrical impedance tomography. *American journal of respiratory and critical care medicine*, 169:791–800, 04 2004.

[82] Zhou Wang, A. C. Bovik, H. R. Sheikh, and E. P. Simoncelli. Image quality assessment: from error visibility to structural similarity. *IEEE Transactions on Image Processing*, 13(4):600–612, 2004.

[83] Y. Zou and Z. Guo. A review of electrical impedance techniques for breast cancer detection. *Medical engineering & physics*, 25:79–90, 04 2003.